Research Square

Preprints are preliminary reports that have not undergone peer review.
They should not be considered conclusive, used to inform clinical practice,
or referenced by the media as validated information.

Global non-cropland soil organic carbon loss risk under multi-level warming scenarios

Keqiang Wang
Xinjiang University
Zipeng Zhang
zp_zhang@xju.edu.cn
Xinjiang University
Xiangyu Ge
Xinjiang University
Lijing Han
Shandong University of Science and Technology
Jingzhe Wang
Shenzhen Polytechnic University
Jianli Ding
Xinjiang Institute of Technology
Lei Zhang
Lawrence Berkeley National Laboratory

Research Article

Keywords: Soil organic carbon, Climate warming, Process-data integration, RothC model, Random Forest, Spatial heterogeneity

Posted Date: August 24th, 2026

DOI: https://doi.org/10.21203/rs.3.rs-10457951/v1

License: This work is licensed under a Creative Commons Attribution 4.0 International License.
Read Full License

Additional Declarations: No competing interests reported.

Global non-cropland soil organic carbon loss risk under multi-level warming scenarios

Keqiang Wang[a,b], Zipeng Zhang[a] ✉, Xiangyu Ge[a], Lijing Han[c], Jingzhe Wang[d], Jianli Ding[e,f], Lei Zhang[g] ✉

[a] *College of Geographical and Remote Sciences, Xinjiang University, Urumqi, 830017, China*

[b] *College of Earth and Environmental Sciences, Lanzhou University, Lanzhou, 266590, China*

[c] *College of Geodesy and Geomatics, Shandong University of Science and Technology, Qingdao, 266590, China*

[d] *School of Artificial Intelligence, Shenzhen Polytechnic University, Shenzhen, 518055, China*

[e] *Xinjiang Institute of Technology, Aksu, 843099, China*

[f] *Institute for Beautiful China, Xinjiang University, Urumqi, 830017, China*

[g] *Climate and Ecosystem Science Division, Lawrence Berkeley National Laboratory, Berkeley, CA, USA*

✉ ***Corresponding author:*** *College of Geographical and Remote Sciences, Xinjiang University, Urumqi, 830017, China;* ***zp_zhang@xju.edu.cn***

Climate and Ecosystem Science Division, Lawrence Berkeley National Laboratory, Berkeley, CA, USA; ***lei.zhang@lbl.gov***

Abstract:

Background Against the backdrop of global warming, soil organic carbon (SOC) plays a critical role in regulating terrestrial carbon storage and climate feedbacks. However, the response mechanisms of SOC to different warming intensities remain insufficiently understood due to the complex interactions among climate conditions, ecosystems, and soil properties. To improve the mechanistic understanding and spatial representation of SOC responses to warming, this study developed a coupled framework integrating the RothC process model with a random forest model to assess SOC responses under multi-gradient warming scenarios across global terrestrial non-cropland ecosystems.

Results Using data from 49,244 global soil sample points, seven temperature-change scenarios were established, including one baseline scenario and six warming scenarios (T5–T30). Six warming scenarios were generated by increasing baseline temperature according to 5–30% of the difference between monthly maximum and mean temperatures. The results indicate that global terrestrial non-cropland SOC in the 0–20 cm soil layer exhibited an overall net loss under all warming scenarios, with SOC losses increasing with warming intensity. From T5 to T30, global SOC stocks decreased by 7.58–17.60 Pg, corresponding to average ΔSOC values of −40.23 to −92.73 g C m^{-2}. Forest ecosystems showed the largest SOC losses (up to 11.88 Pg), followed by grasslands and shrublands. Negative SOC responses were mainly concentrated in mid-to-high latitude and high-altitude regions, including northern North America, northern Eurasia, and the Qinghai–Tibet Plateau. Driving factor analysis revealed that net primary productivity and mean annual temperature were the dominant predictors, indicating the contributions of ecosystem carbon inputs and temperature-driven decomposition processes to SOC responses. Soil properties related to carbon stabilization capacity also contributed substantially to explaining SOC variations across land-cover types.

Conclusion This study demonstrates that warming-induced SOC responses are regulated by the balance among carbon inputs, decomposition losses, and soil carbon stabilization processes. The coupled process-data framework improves the integration of mechanistic constraints and spatial prediction capability, providing new insights into

global SOC responses to climate warming and supporting regional carbon management under changing climate conditions.

Keywords: Soil organic carbon; Climate warming; Process-data integration; RothC model; Random Forest; Spatial heterogeneity

1. Introduction

Against the backdrop of global warming, soil, as the largest carbon reservoir in terrestrial ecosystems, plays a pivotal role in the transition between carbon sink and carbon source. It is estimated that approximately 684–1190 Pg of organic carbon is stored in the 0–30 cm soil layer (Batjes, 2014), representing a carbon pool comparable in magnitude to the combined atmospheric and vegetation carbon pools. At the global scale, cropland covers about 1.6 billion ha, accounting for only approximately 12% of the world's land area; thus, land areas other than cropland constitute the dominant component of the terrestrial surface (FAO, 2025). Therefore, even minor changes in soil organic carbon (SOC), particularly across extensive non-cropland ecosystems, can have a significant impact on atmospheric CO_2 concentrations, thereby further influencing the stability and feedback processes of the global climate system (Minasny et al., 2017).

Previous studies have shown that rising temperatures can affect soil organic carbon stocks through multiple mechanisms. On the one hand, rising temperatures enhance microbial activity, accelerate the decomposition of soil organic matter, and lead to increased SOC mineralization rates (Davidson and Janssens, 2006); on the other hand, in certain regions, warmer climates may promote plant growth and carbon input, thereby mitigating carbon loss to some extent (van Gestel et al., 2018). This dual mechanism results in significant regional heterogeneity in SOC's response to warming, with both potential carbon sources and potential carbon sinks existing (Bradford et al., 2016). For non-cropland ecosystems, such warming-induced SOC responses are especially important because these areas include extensive forests, grasslands, shrublands, and sparsely managed natural or semi-natural landscapes, where SOC dynamics are primarily regulated by climate, vegetation productivity, soil properties, and topography rather than direct agricultural management (Davidson and Janssens,

2006; Bradford et al., 2016; Crowther et al., 2016). Therefore, accurately assessing the response patterns of SOC in non-cropland areas to varying degrees of climate warming on a global scale is one of the key tasks for understanding terrestrial carbon cycle dynamics and predicting climate change trends.

In recent years, numerous studies have explored the mechanisms underlying SOC responses to climatic factors using methods such as field observations, controlled experiments, and model simulations. For example, a 26-year soil warming experiment (+5°C) conducted in the Harvard Forest in the United States showed that the annual SOC loss rate reached 1.2% during the first 10 years of warming, subsequently slowing to 0.3% due to microbial substrate limitation, demonstrating significant time dependence (Melillo et al., 2017). A meta-analysis by the International Warming of Permafrost Experiment network found that a 2°C warming in the Arctic increases the decomposition rate of surface SOC by 35–60%, but carbon release from deep permafrost exhibits a 3–5-year lag (Schuur et al., 2015). Although controlled warming experiments provide direct evidence for the mechanisms by which temperature regulates SOC decomposition and stabilization, their application at large spatial scales remains limited. Most warming experiments are conducted at specific sites, under particular vegetation, soil, and climatic conditions, and their experimental duration, warming magnitude, soil depth, and treatment design often differ among studies. These differences make it difficult to directly extrapolate site-level experimental results to regional or global scales, especially for heterogeneous non-cropland ecosystems. Therefore, large-scale assessments require modeling frameworks that can integrate mechanistic understanding from process-based models with spatially explicit environmental information. In terms of modeling, process models such as CENTURY, RothC, and DNDC are widely used for soil carbon simulation across various ecosystems. Among these, the RothC model, characterized by its simple structure, minimal parameter requirements, and high adaptability, has been successfully applied in a wide range of global ecosystems (Coleman and Jenkinson, 1996).

Process-oriented (PO) models are constructed based on an in-depth understanding of SOC cycling processes and their interactions with environmental factors. By

simulating the biogeochemical processes of soil organic matter decomposition, synthesis, and transformation, as well as carbon and nutrient cycling, these models can more accurately reflect the dynamic changes in SOC over time (Zhang et al., 2020). However, when applied at the global scale, traditional PO models face challenges such as insufficient regional representativeness of parameters and limitations in model structural generality (Zhang et al., 2024). Random Forest (RF), as an ensemble learning method, excels at handling high-dimensional nonlinear problems and has demonstrated strong performance in fields such as climate ecology and soil modeling (Mulder et al., 2016). With the development of emerging modeling methods such as machine learning, an increasing number of researchers are attempting to combine statistical learning with process modeling to enhance the predictive capabilities of models under conditions of large-scale spatial heterogeneity (Zhang et al., 2024; Zhang et al., 2023a). However, existing process–data fusion studies have mainly focused on improving the spatial mapping and prediction accuracy of SOC stocks or SOC contents, while relatively less attention has been paid to the spatially explicit response of SOC to warming perturbations (Lamichhane et al., 2019; Zhang et al., 2024). In particular, it remains unclear how SOC in global terrestrial non-cropland ecosystems responds to different magnitudes of warming, how such responses vary across land cover types and climate regions, and which environmental factors dominate the spatial heterogeneity of warming-induced SOC changes (Bradford et al., 2016; Crowther et al., 2016). Therefore, there is still a need to shift from static SOC mapping toward scenario-based SOC response assessment by explicitly coupling process-based warming simulations with machine-learning spatial extrapolation (Zhang et al., 2024; Bernardini et al., 2024).

This study aims to establish an integrated assessment framework combining process models with machine learning to systematically analyze the response characteristics of SOC to multi-gradient climate warming scenarios. Specifically, we exclude agricultural land, wetlands, and water bodies at the global scale (existing RothC model studies have primarily focused on areas with significant human activities, such as farmland, while systematic assessments of soil carbon responses across large-scale terrestrial non-cropland areas remain relatively scarce). We constructed 7 temperature

change scenarios (ranging from no temperature change to a 30% increase, with 5% increments) and input these temperature parameters into the RothC model to simulate SOC over a one-year period, obtaining the spatial distribution of SOC under different temperature conditions. Subsequently, by calculating the SOC difference between each warming scenario and the baseline scenario, soil carbon response values (ΔSOC) were derived. These values, combined with environmental covariates (such as climatic factors, topography, soil properties, and vegetation indices), were input into a random forest model to fit the distribution patterns and dominant controlling factors of global ΔSOC, ultimately generating spatial predictions of SOC responses for different global warming scenarios.

The main innovations of this study are as follows: (1) A process-data fusion framework coupling the RothC process model with the Random Forest model was established, balancing the expression of SOC response mechanisms with spatial extrapolation capabilities; (2) A multi-gradient warming simulation framework for SOC dynamics was proposed to comprehensively capture the spatial distribution, regional divergence and uncertainty of SOC variations over global non-agricultural lands.

2. Materials and Methods

2.1 Data Collection and Preprocessing

Initial SOC values and related soil property data were obtained from the World Soil Information Service (WoSIS) snapshot – September 2019 dataset (Batjes et al., 2020). This dataset integrates large-scale global soil profile observations and has undergone standardization and quality control. It provides key soil physicochemical properties at various depths (0–200 cm), including organic carbon content, texture composition (proportions of sand, silt, and clay), pH, and bulk density. The sampling depths of the soil profiles used in this study are based on soil horizon classifications or fixed depth intervals; therefore, soil layer depths vary across different sampling points. To address the issue of inconsistent soil layer depths, we divided the data into five depth intervals (0 – 20 cm, 20 – 40 cm, 40 – 80 cm, 80 – 100 cm, 100 – 200 cm) and fitted all soil profiles using an equal-area spline function (Malone et al., 2009). Furthermore, we used

the "mpspline2" package (version 0.1.6) in R version 4.4.0 to perform equal-area spline function fitting, with the smoothing parameter λ set to the default value of 0.1.

In this study, SOC content was extracted from the 0–20 cm soil layer, and the corresponding density was obtained according to Eq. (1).

$$SOCdensity = \{\frac{(SOC \times BD \times SD)}{100}\} \times \{1 - \frac{CF}{100}\} \quad (1)$$

where SOC density represents soil organic carbon density (kg C m^{-2}); SOC represents soil organic carbon content (g kg^{-1}); BD represents bulk density (kg dm^{-3}); SD represents soil layer thickness (cm); and CF represents the coarse fragment content (%).

The spatial scope of this study covers global terrestrial non-cropland areas. Before model simulation and spatial prediction, croplands, wetlands, bare ground, and water bodies were excluded from the study domain. For croplands, SOC dynamics are strongly influenced by agricultural management practices, including tillage, fertilization, irrigation, residue return, crop rotation, and harvest removal. Representing these processes requires detailed and region-specific management information, which is difficult to harmonize at the global scale and falls outside the temperature-focused scenario design of this study (Morais et al., 2019). Wetlands were not included because the standard RothC model is designed for non-waterlogged topsoil and does not explicitly represent persistent water saturation, anaerobic decomposition, water-table fluctuations, or methane-related carbon cycling. Directly applying RothC to wetland soils may therefore introduce considerable structural uncertainty (Trettin et al., 2001). Water bodies do not represent terrestrial soil systems targeted by RothC and were consequently excluded. Bare ground was also excluded because of its sparse vegetation cover and limited representation of plant-derived carbon inputs (Coleman and Jenkinson, 1996). Land cover data were sourced from Land Cover (GLCNMO)–Global version (500 m resolution); based on its classification codes, samples were excluded from cropland (codes: 11–13), wetlands (code: 15), bare ground (codes: 16–17), and water bodies (codes: 19–20). Prior to processing, all data were projected to WGS84 in ArcGIS 10.8 and uniformly resampled to a spatial resolution of 0.05° × 0.05° to ensure

consistency among multi-source data and computational efficiency. After excluding redundant areas, a total of 49,244 soil sample points remained. Among these, 32,623 were from forest areas, 9,963 from grassland areas, and 6,658 from shrubland areas (Fig. 1).

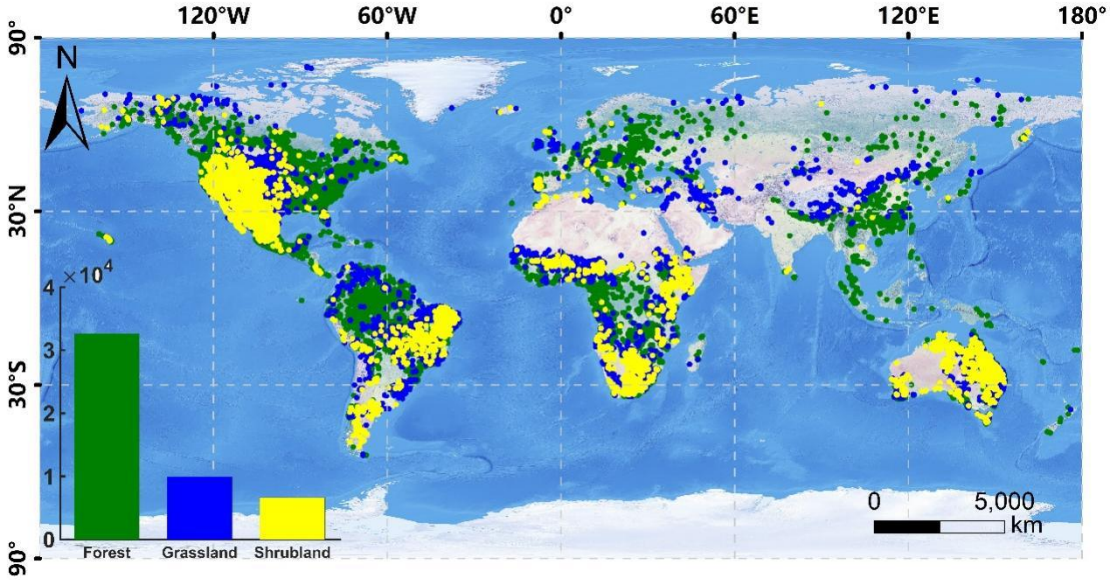


Fig. 1. Schematic diagram of the global distribution of soil sample points based on land cover types.

2.2 Model Calibration and Point-Scale Response Analysis

2.2.1 Scenario Design

Scenario-based warming simulations have been widely used in process-based SOC modeling to assess the sensitivity of soil carbon pools to climate warming under different climate assumptions (Gottschalk et al., 2012; Wiesmeier et al., 2016). Recent studies have further adopted multi-gradient warming scenarios combined with RothC and machine-learning models to quantify SOC responses across different warming intensities (Zhou et al., 2025). Therefore, this study designed seven temperature change scenarios to systematically assess the response of global non-cropland SOC to climate warming. The seven scenarios included one baseline scenario (0% warming) and six warming scenarios (T5–T30), and only temperature was altered while other environmental factors were held constant across all scenarios. The scenarios were based on current climate conditions, simulating possible future warming scenarios by setting

different magnitudes of temperature increases. The specific settings are as follows: Using historical climate data from 1960–2014 as a baseline, temperature conditions were kept constant (0% warming) to serve as the reference for comparative analysis. Warming scenarios were simulated by increasing temperatures by 5%, 10%, 15%, 20%, 25%, and 30% relative to the baseline scenario (Table 1), covering a range from mild to significant warming. The temperature change for each scenario was calculated based on the difference between the maximum and average monthly temperatures (ΔTmax-avg) for the periods 1960–1980 and 1981–2014. Temperature changes were calculated using Eq. (2) below:

$$\Delta T = (T_{max} - T_{avg}) \times r \quad (2)$$

where T_{max} and T_{avg} represent the monthly maximum temperature and monthly average temperature, respectively, with data sourced from the Google Earth Engine platform (https://earthengine.google.com/); r denotes the percentage increase in temperature (5%, 10%, ..., 30%). To analyze the impact of temperature on SOC in isolation, other environmental factors (such as precipitation, vegetation cover, and soil texture) were held constant across all scenarios.

Table 1. Parameters for each warming scenario; T_{max} and T_{avg} represent the monthly maximum temperature and monthly average temperature, respectively.

Scenario	Warming Magnitude
T5	$(T_{max} - T_{avg}) \times 5\%$
T10	$(T_{max} - T_{avg}) \times 10\%$
T15	$(T_{max} - T_{avg}) \times 15\%$
T20	$(T_{max} - T_{avg}) \times 20\%$
T25	$(T_{max} - T_{avg}) \times 25\%$
T30	$(T_{max} - T_{avg}) \times 30\%$

2.2.2 RothC Model Simulation

The PO model selected for this study is the RothC-26.3 model, which is designed to simulate SOC turnover (Coleman and Jenkinson, 1996). The RothC model was developed by Jenkinson in 1977 based on long-term plot data from the Rothamsted Research Station in the UK (Zhao et al., 2016). Simulating SOC changes by modeling

carbon decomposition and accumulation processes has been widely used to simulate the spatiotemporal dynamics of organic carbon (Dechow et al., 2019).

In the RothC model, organic carbon is divided into four active pools: degradable plant material (DPM), resistant plant material (RPM), humified organic matter (HUM), microbial biomass (BIO), and one inactive pool—a small amount of inert organic matter (IOM). IOM does not participate in the carbon cycle (Falloon et al., 1998), and its calculation formula is given in Eq. (3):

$$IOM=0.049\times SOC^{1.139} \quad (3)$$

When carbon enters different types of vegetation, it is divided into DPM and RPM, with the specific allocation ratio depending on the plant's DPM/RPM ratio. The DPM/RPM ratio for forests is typically set at 0.25, while for grasslands and shrublands it is set at 0.67 (Coleman and Jenkinson, 1996). The decomposition of DPM and RPM produces CO_2, BIO, and HUM, the proportions of which are influenced by the clay content in the soil (Wang et al., 2022); see Eq. (4) for details. BIO and HUM will undergo further decomposition in subsequent processes, generating additional CO_2, BIO, and HUM.

$$x=1.67\times(1.85+1.60\times e^{-0.0786.Clay}) \quad (4)$$

Here, x represents the ratio of CO_2 to the sum of BIO and HUM, and Clay denotes the percentage of clay content in the soil. Then, $x/(x+1)$ represents CO_2 release, while $1/(x+1)$ represents the formation of BIO + HUM.

The decomposition process in each active pool follows first-order decay kinetics and is influenced by temperature, moisture, and soil cover, as shown in Eq. (5):

$$\Delta Z=Z(1-e^{-abckt}) \quad (5)$$

Z is the SOC stock in the active pool; ΔZ is the monthly loss of SOC in the active pool; *a, b, and* c are rate-adjustment factors for temperature, moisture, and soil cover, respectively; their equations can be found in ; k is the decomposition rate constant of the active pool: the values for the DPM, RPM, BIO, and HUM pools are 10, 0.3, 0.66, and 0.02, respectively; t is 1/12 (Coleman and Jenkinson, 1996).

Table 2. Parameters required for the RothC model.

	Covariate	Unit	Time	Reference
Initialization	Clay content	g kg^{-1}		https://soilgrids.org
	Temperature	°C	1960-1980	https://cds.climate.copernicus.eu/
	Precipitation	mm	1960-1980	https://cds.climate.copernicus.eu/
	Evapotranspiration	mm	1960-1980	https://cds.climate.copernicus.eu/
	SOC	Mg C ha^{-1}	1918-2016	https://data.isric.org/
	Input carbon	Mg C ha^{-1}	1960-2016	This study
	NDVI		1981-2020	https://www.earthdata.nasa.gov/
Forward	Clay content	g kg^{-1}		https://soilgrids.org
	Temperature	°C	1981-2016	https://cds.climate.copernicus.eu/
	Precipitation	mm	1981-2016	https://cds.climate.copernicus.eu/
	Evapotranspiration	mm	1981-2016	https://cds.climate.copernicus.eu/
	SOC	Mg C ha^{-1}	1918-2016	https://data.isric.org/
	Input carbon	Mg C ha^{-1}	1981-2016	This study
	NDVI		1981-2020	https://www.earthdata.nasa.gov/

When simulating SOC using the RothC model, the following data are primarily required: monthly climate data (including precipitation, average temperature, and potential evapotranspiration), initial SOC content, carbon inputs, Normalized Difference Vegetation Index (NDVI) (used to determine vegetation cover), and soil clay content (Table 2). When simulating SOC changes under different scenarios, we divided the data into seven tables based on the defined scenarios, and then further subdivided these seven tables by land cover type for model input. The RothC model simulation involves at least two stages: the initialization stage and the forward run stage (Gottschalk et al., 2012; Smith et al., 2005; Smith et al., 2007). The initialization phase typically involves running the model for an extended period under constant climate and carbon input conditions until the model reaches a steady state, thereby calculating the sizes of the various SOC pools and annual plant carbon inputs. In this study, the model was run for 1,000 years at each sampling point across the three land cover types to achieve a steady state. During this process, climate parameters were derived from historical monthly average climate data for the 1960–1980 period (with temperature data adjusted according to the scenario, while other climate parameters remained

constant), and the initial annual carbon input was set to the model's default value. Carbon inputs were adjusted based on the difference between simulated and observed SOC (Smith et al., 2005), as shown in Eq. (6):

$$C_{eq}=C_i\times(SOC-IOM)/(SOC_{simf}-IOM) \quad (6)$$

Here, C_i is the carbon input in the initial year of the model's default parameters, and C_{eq} is the carbon input required to reach equilibrium; SOC and $SOCS_{simf}$ represent the observed SOC in the initial year (Xu et al., 2019), and the simulated SOC after the first equilibrium run, respectively; IOM denotes the carbon content of the inert organic matter (IOM) fraction.

The soil transfer function (Weihermüller et al., 2013) was used to estimate the sizes of different SOC pools at equilibrium, as shown in Eqs. (7), (8), and (9).

$$\mathrm{RPM}=(0.1847\times SOC+0.1555)\times(clay+1.2750)^{-0.1158} \quad (7)$$

$$\mathrm{HUM}=(0.7148\times SOC+0.5069)\times(clay+0.3421)^{0.0184} \quad (8)$$

$$\mathrm{BIO}=(0.0140\times SOC+0.0075)\times(clay+8.8473)^{0.0567} \quad (9)$$

Where SOC is the observed SOC in the starting year, and $Clay$ represents the percentage of clay content in the soil.

Once the carbon input required to reach equilibrium C_{eq} and the carbon stocks in each SOC pool have been determined, the model can proceed to the forward simulation phase. Given the long temporal span of SOC data, this study utilized monthly average climate inputs from 1981 to 2014 (with temperature data adjusted according to different scenarios while other climate parameters remained constant) to simulate SOC dynamics for the following period. Ideally, carbon inputs for this phase should be derived from time series data on plant residues and fertilizers; however, detailed information on these variables was not available in this study. Therefore, we collected NPP data for 1981–2014 (https://www.glass.hku.hk/download.html), and calculated the averages for NPP in the periods 1981–1997 and 1998–2014, respectively, assuming that soil carbon input is proportional to NPP (Gottschalk et al., 2012; Smith et al., 2005). Based on the carbon input required at equilibrium, C_{eq}, changes in NPP during the simulation period are calculated using Eq. (10) to adjust the carbon input for the following year. This method indirectly and partially accounts for the effects of different plant species and

regions (Smith et al., 2005; Wang et al., 2022).

$$Cinput_t=(NPP_t/NPP_{t-1})\times Cinput_{t-1} \quad (10)$$

where NPP_t is the NPP in year t; NPP_{t-1} is the NPP in the previous year; $Cinput_t$ is the carbon input in year t; $Cinput_{t-1}$ is the carbon input in the previous year; when $t=0$, $Cinput_{t-1}$ refers to the carbon input C_{eq} at model equilibrium. The above simulations and numerical analyses were implemented using the Python programming language to simulate SOC time series.

2.3 Spatial Modeling and Driving Factor Analysis of SOC Changes

2.3.1 Random Forest

RF is a tree-based machine learning method that achieves regression and classification predictions for target variables by constructing a set of regression trees and averaging their predictions (Breiman, 2001). Over the past decade, RF has been one of the most commonly used machine learning models in the field of digital soil mapping (Mishra et al., 2020). Based on the results of seven scenario simulations from the RothC model, this study first calculated the difference between each of the six warming scenarios and the baseline scenario to obtain ΔSOC. Subsequently, because ΔSOC often exhibits a heavy-tailed distribution on a global scale, extreme values may be caused by an amplification effect resulting from spatial mismatch errors between process model outputs and input data, as well as errors in initial carbon input estimates. Such high-leverage samples can significantly affect the stability of a random forest's learning of the overall relationship (Rousseeuw and Hubert, 2011). To reduce the dominant effect of outliers on model training, this study applied quantile truncation to the target variable ΔSOC, removing the lowest 5% of values on the decreasing end and the highest 1% on the increasing end. Under the condition where only temperature perturbations are altered while other factors remain constant, the process of significant SOC increases is more constrained, whereas the dispersion and fat-tailed phenomena at the decreasing end are more pronounced. Therefore, a strategy of stricter cutoff at the decreasing end and a wider range at the increasing end is adopted to obtain a more robust fitting relationship and spatial prediction results. After processing, the model's output of

ΔSOC and relevant environmental covariates were selected for RF modeling. During modeling, the number of trees was set to 500 (Zhang et al., 2021; Zhang et al., 2023b). Node selection used the model's default parameters, with the maximum number of features set to one-third of the total number of features, rounded down.

This study extracted 15 environmental covariates directly or indirectly related to SOC turnover from soil data points as feature variables (see Table 3) (Moura-Bueno et al., 2021), including four major categories: climatic factors, soil properties, topographic factors, and vegetation. Due to potential multicollinearity among environmental covariates, this study employed variance inflation factor (VIF) analysis to address this issue (Kasraei et al., 2024), with Eq. (11) defined as follows:

$$VIF_i = 1/(1-R_i^2) \tag{11}$$

where VIF_i is the variance inflation factor for the i-th independent variable. R_i^2 is the coefficient of determination (i.e., R^2) obtained from the regression equation of the i-th independent variable against all other independent variables. Generally, if VIF > 10, the multicollinearity issue between that variable and the others is considered severe, and variable screening should be considered (Craney and Surles, 2002). Testing should then continue until the multicollinearity of the remaining environmental covariates is <10. After processing, no environmental covariates with excessive multicollinearity were found. Upon completion of this step, we set the target variable to the ΔSOC for each scenario and trained the RF model with environmental covariates as predictors, followed by 10-fold cross-validation. The above operations were implemented in RStudio using the randomForest and shapviz packages.

In this study, the following three metrics were selected to evaluate model accuracy: the coefficient of determination (R^2), root mean square error (RMSE), and mean absolute error (MAE). A higher R^2 value, along with lower RMSE and MAE values, indicates better model accuracy.

369 **Table 3.** Environmental covariates after VIF testing.

Environmental factors class	Covariate	Abbreviation	Unit	VIF	Time	Reference
Topographic	profile curvature	PRC	m	1.74	2000	(JPL, 2013)
Topographic	Aspect	Aspect	°	1.03	2000	(JPL, 2013)
Topographic	Slope	Slope	°	1.95	2000	(JPL, 2013)
Topographic	Elevation	Elev	m	2.02	2000	(JPL, 2013)
Topographic	Landform	Landform		2.62	2008	https://esdac.jrc.ec.europa.eu/content/global-landform-classification
Climate	Annual mean precipitation	AMP	mm	2.82	1960-2014	https://cds.climate.copernicus.eu/
Climate	Annual mean temperature	AMT	℃	4.00	1960-2014	https://cds.climate.copernicus.eu/
Climate	Annual mean potential evapotranspiration	AME	mm	5.49	1960-2014	https://cds.climate.copernicus.eu/
Soil	Cation exchange capacity	CEC	cmol kg^{-1}	1.49		https://soilgrids.org
Soil	Silt content	Silt	g $100g^{-1}$	1.66		https://soilgrids.org
Soil	Soil pH in H_2O	Phh2o		2.93		https://soilgrids.org
Soil	Bulk Density of the fine earth fraction	BD	kg dm^{-3}	2.91		https://data.isric.org/
Soil	Coarse Fragments Volumetric fraction	CFVO	cm^3 $100cm^{-3}$	1.37		https://data.isric.org/
Vegetation	Normalized difference vegetation index	NDVI		4.65	1981-2022	https://www.earthdata.nasa.gov/
Vegetation	Net primary production	NPP	g C m^{-2}	4.85	1980-2020	https://glass-product.bnu.edu.cn/

370

2.3.2 SHAP Analysis and Marginal Effects

The Shapley Additive Explanations (SHAP) method is an algorithm used to interpret the predictions of complex models (Lundberg and Lee, 2017). Drawing on game theory, SHAP values decompose changes in prediction results across individual feature variables, reflecting the direction and magnitude of positive or negative contributions from different features to the model's output. In this study, we used this method to obtain a global SHAP importance ranking and further plotted SHAP feature importance ranking plots and SHAP feature contribution plots to analyze the response patterns of key factors.

Furthermore, this study incorporates marginal effect analysis into the model interpretation phase to characterize the nonlinear relationship between key environmental factors and ΔSOC, and employs partial dependence plots to visualize these marginal effects. Partial dependence plots estimate the average response trend of the model's predicted values when a specific target variable varies, by fixing the range of that variable's values and averaging the remaining variables (Friedman, 2001; Goldstein et al., 2015). Marginal effect curves were plotted for variables with high SHAP rankings and clear ecological significance to observe their response direction, magnitude of change, and potential threshold characteristics. These operations were performed in RStudio using the shapviz package.

This study also calculated variable importance using random forests to compare differences in dominant factors across different land cover types and warming scenarios. Variable importance reflects the relative contribution of covariates to the model's predictive power (Louppe et al., 2013). This study employs a consistent feature set and modeling workflow to calculate importance across scenarios, and conducts cross-comparisons after normalization. In comparing differences among land cover types, this study groups data into forest, grassland, and shrubland categories, aggregates the importance results for each group, and presents the difference structures using stacked bar charts and grouped bar charts. These operations were performed in the R environment.

2.3.3 Uncertainty Analysis

Uncertainty refers to the degree of uncertainty in model predictions or estimates (Karhu et al., 2012). Even well-validated models exhibit uncertainty in their outputs. This is because the explanatory ability of the model may be constrained by the selected covariates, which may not fully represent all environmental predictors controlling SOC changes. Therefore, model predictions should be presented alongside their associated uncertainty intervals to support decision-making (Qin et al., 2016).

To assess the spatial uncertainty of model predictions, this study used a quantile regression forest (QRF)-based uncertainty estimation approach (Zhang et al., 2025). For each grid cell, QRF was used to estimate the conditional distribution of predicted ΔSOC and to extract the 5th percentile ($Q_{0.05}$), median ($Q_{0.50}$), and 95th percentile ($Q_{0.95}$). These three quantiles were then used to calculate the prediction interval ratio (PIR), following Eq. (12):

$$PIR = \frac{|Q_{0.95} - Q_{0.05}|}{|Q_{0.50}|} \tag{12}$$

where $Q_{0.05}$ and $Q_{0.95}$ represent the lower and upper limits of the 90% prediction interval, respectively, and $Q_{0.50}$ represents the median prediction. The denominator was expressed as an absolute value to avoid negative PIR values when predicted ΔSOC values were negative. A larger PIR indicates a wider relative prediction interval and therefore higher prediction uncertainty. Finally, a global spatial distribution map of PIR was generated to identify regions with high uncertainty in predicted SOC responses, thereby providing a reference for result interpretation and model improvement.

2.4 Differences in SOC Responses to Climate Warming

2.4.1 Spatial Mapping Evaluation Methods

After training and validating the random forest models under each warming scenario, this study applies the corresponding models to global-scale gridded covariate data to conduct spatial predictions of ΔSOC. In practice, the study invokes the corresponding random forest models for each of the six warming scenarios (T5 to T30). After inputting covariates for each valid pixel, the models output predicted ΔSOC values, ultimately

generating global ΔSOC raster maps for the six scenarios. The mapping process for each scenario uses the same set of covariates, the same spatial framework, and the same mask coverage; the only difference is the warming scenario corresponding to the target variable.

After completing the spatial prediction, the study also conducted a basic spatial plausibility check on the results. The check included the spatial continuity of the prediction maps, whether changes along major environmental gradients were smooth, and whether locally anomalously high values or abrupt change regions coincided with land-use boundaries, data-missing areas, or regions with high input errors.

2.4.2 Technical workflow

Overall, the methodological framework of this study integrates data preprocessing, RothC-based point-scale scenario simulation, random forest spatial prediction, driver interpretation, and uncertainty assessment. The complete technical workflow is summarized in Fig. 2.

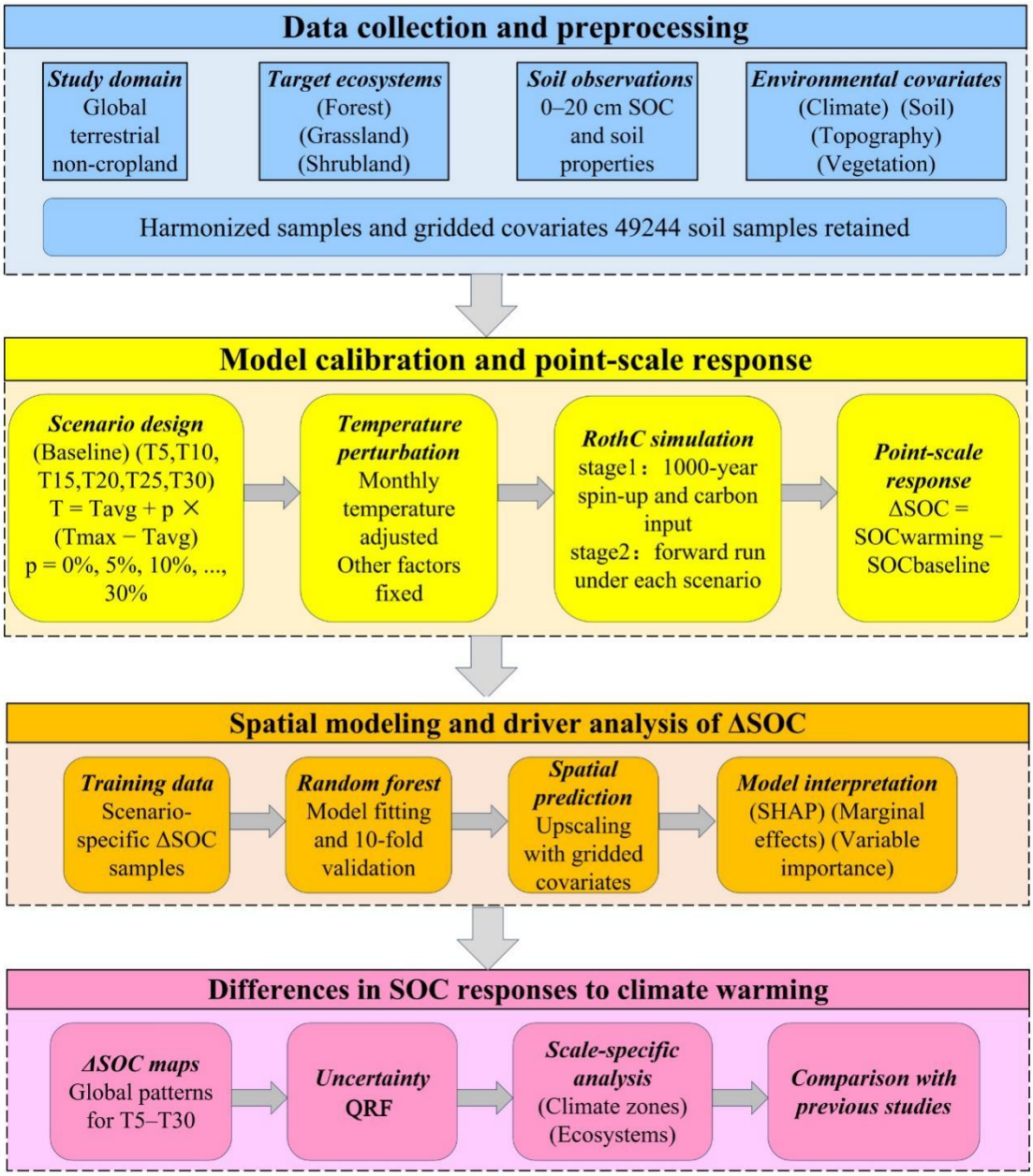


Fig. 2. Technical workflow diagram.

3. Results

3.1 Point-Scale SOC Warming Response Characteristics

Fig. 3 shows that, under the six warming scenarios, the global point-scale ΔSOC in non-cropland areas is predominantly negative, with the density peaks of each scenario primarily distributed below 0. This indicates that, under conditions where only temperature is altered, SOC generally decreases. As the warming scenarios intensify from T5 to T30, the center of the ΔSOC distribution gradually shifts toward negative

values, with the mean decreasing from approximately −43 g C m^{-2} in T5 to approximately −102 g C m^{-2} in T30, indicating that the magnitude of SOC loss continues to increase with intensifying warming. At the same time, the left tail of the distribution curve is longer under high warming scenarios, indicating a stronger negative SOC response at some sampling points.

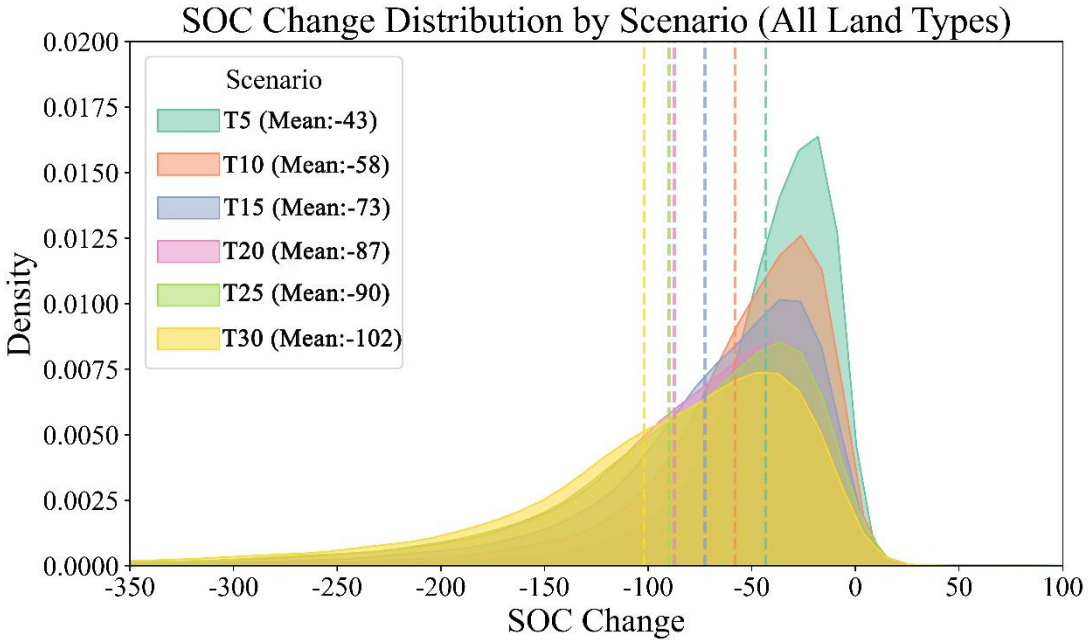


Fig. 3. Kernel density distributions of ΔSOC at the site scale for global non-cropland under six warming scenarios. Dashed lines indicate the mean values for each scenario.

Fig. 4 shows significant differences in the distribution of ΔSOC across different land cover types. Forest land cover (Fig. 4(a)) exhibited the greatest SOC loss, with the mean value decreasing from approximately −51 g C m^{-2} in T5 to approximately −118 g C m^{-2} in T30 across all six scenarios, and a longer negative tail, indicating that forest sites are more sensitive to warming disturbances. Grasslands and shrublands (Fig. 4(b), Fig. 4(c)) also exhibit a trend of increasing losses with rising temperatures, but the overall magnitude is smaller than that of forests; specifically, the mean for grasslands decreases from approximately −32 g C m^{-2} to approximately −76 g C m^{-2}, while the mean for shrublands decreases from approximately −27 g C m^{-2} to approximately −65 g C m^{-2}. All three land cover types exhibited net SOC losses under all warming scenarios, with the intensity of losses generally being highest for forests, followed by grasslands and shrublands.

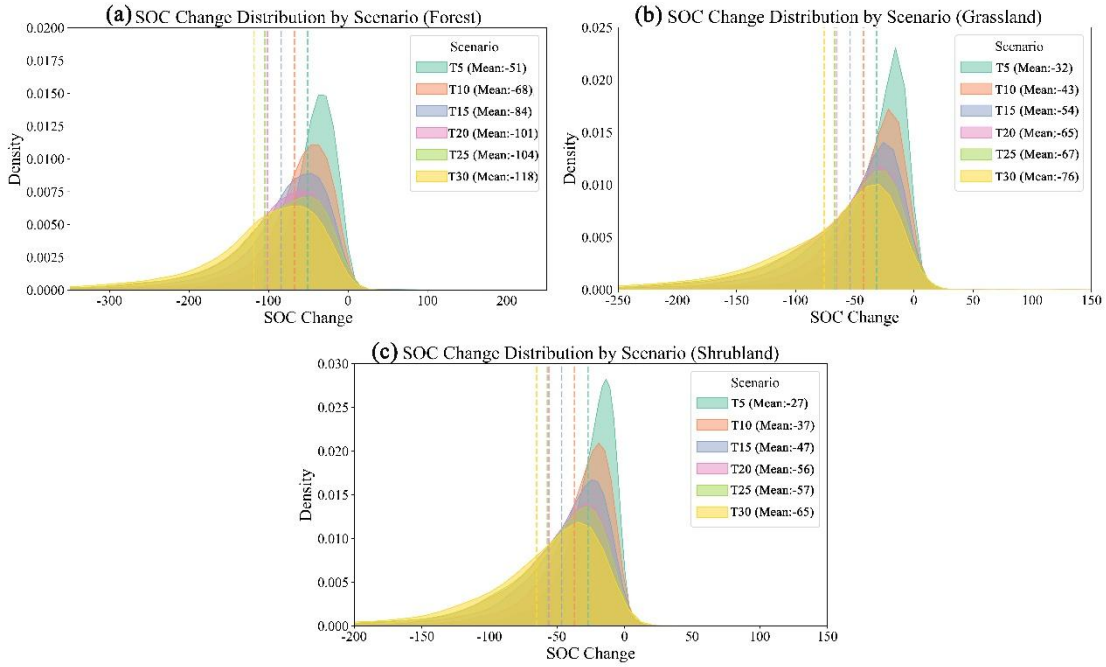


Fig. 4. Kernel density distributions of point-scale ΔSOC for different land cover types under six warming scenarios. (a)–(c) represent forests, grasslands, and shrublands, respectively; dashed lines indicate scenario-specific mean values.

Figs. 5 and 6 show that ΔSOC at sample sites across land cover types exhibits distinct spatial variations along both latitudinal and longitudinal axes under different warming scenarios. Latitudinal profile results (Fig. 5) indicate that ΔSOC for all land cover types is predominantly negative across the six scenarios. Under the T5 scenario (Fig. 5(a)), ΔSOC for forests, grasslands, and shrublands mostly ranges between approximately −150 and 0 g C m^{-2}, with strong negative responses observed in the mid-to-high latitudes of the Northern Hemisphere (approximately 50°N–80°N) and the mid-latitudes of the Southern Hemisphere (approximately 30°S–45°S), with local latitudinal zones potentially falling below −200 g C m^{-2}. As warming intensifies to T10 and T15 (Fig. 5(b), Fig. 5(c)), the curves for the three land cover types shift overall toward negative values, and SOC losses gradually deepen in the mid-to-high latitude regions of the Northern Hemisphere (approximately 40°N–80°N, especially near 55°N–70°N) and the mid-latitude regions of the Southern Hemisphere (approximately 30°S–45°S). By the T20–T30 scenarios (Fig. 5(d)–Fig. 5(f)), ΔSOC for forests and grasslands in the latitudinal bands around 30°S–45°S and 50°N–75°N can reach approximately −200 to

−300 g C m^{-2}, while shrublands also exhibit a significant negative response near 40°S–30°S and 50°N–65°N. This indicates that SOC losses vary significantly along the latitudinal axis, and that the negative response in mid-to-high latitude regions is further amplified under high-warming scenarios.

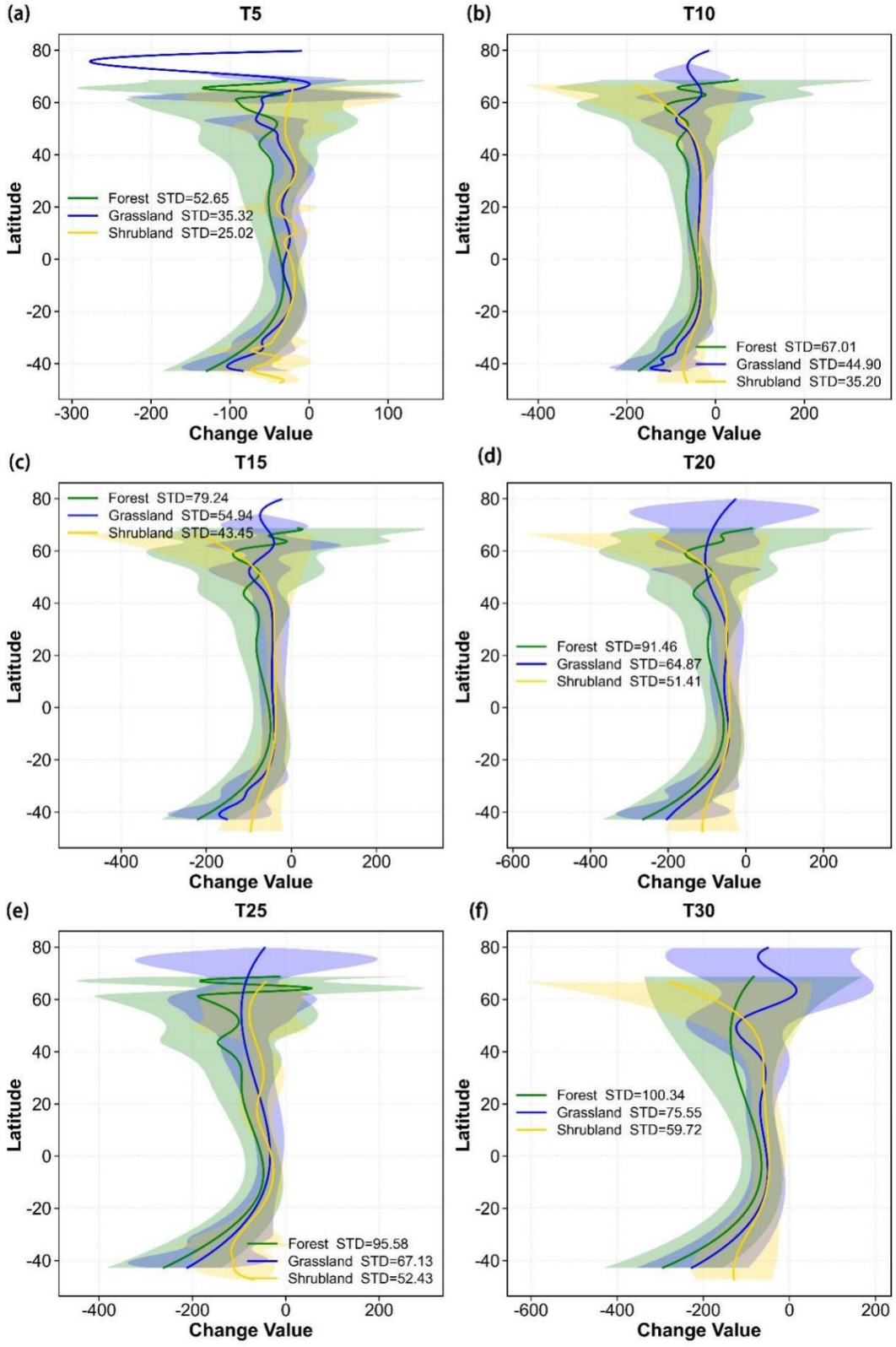


Fig. 5. Fitted profiles of point-scale ΔSOC along the latitudinal gradient for different land cover types under six warming scenarios. Panels (a)–(f) represent the T5, T10, T15, T20, T25, and T30 scenarios, respectively; curves of different colors represent forests, grasslands, and shrublands. Shaded areas with different colors indicate the standard deviation ranges of the corresponding land cover types.

Longitudinal profile results indicate (Fig. 6) that ΔSOC for all land cover types also exhibits significant fluctuations along the longitudinal axis. Under the T5 scenario (Fig. 6(a)), across most of the longitude range from approximately 160°W to 160°E, ΔSOC primarily ranges between approximately −150 and 20 g C m^{-2}, with forests and grasslands exhibiting significant SOC losses in the western longitude region (approximately 160°W–120°W) and in certain longitude bands near the high-value zone in the eastern longitude region (approximately 100°E–160°E), where local values fall below −150 g C m^{-2}. Under the T10 and T15 scenarios (Fig. 6(b) and Fig. 6(c)), most land cover types across most longitude zones still exhibit predominantly negative values, with the negative response of grasslands and shrublands primarily concentrated in the range of approximately −50 to −150 g C m^{-2}. Significant declines are most frequently observed near approximately 160°W–110°W, 90°E–110°E, and 120°E–160°E. As warming intensifies to T20–T30 (Fig. 6(d)–Fig. 6(f)), the negative response deepens across a wider range of longitudes. SOC losses in forests are particularly pronounced near approximately 150°W and 120°E–160°E, with values below −200 g C m^{-2} in some areas; grasslands and shrublands also exhibited decreases of approximately −100 to −200 g C m^{-2} in longitude bands such as 150°W–110°W, 90°E–110°E, and 130°E–160°E.

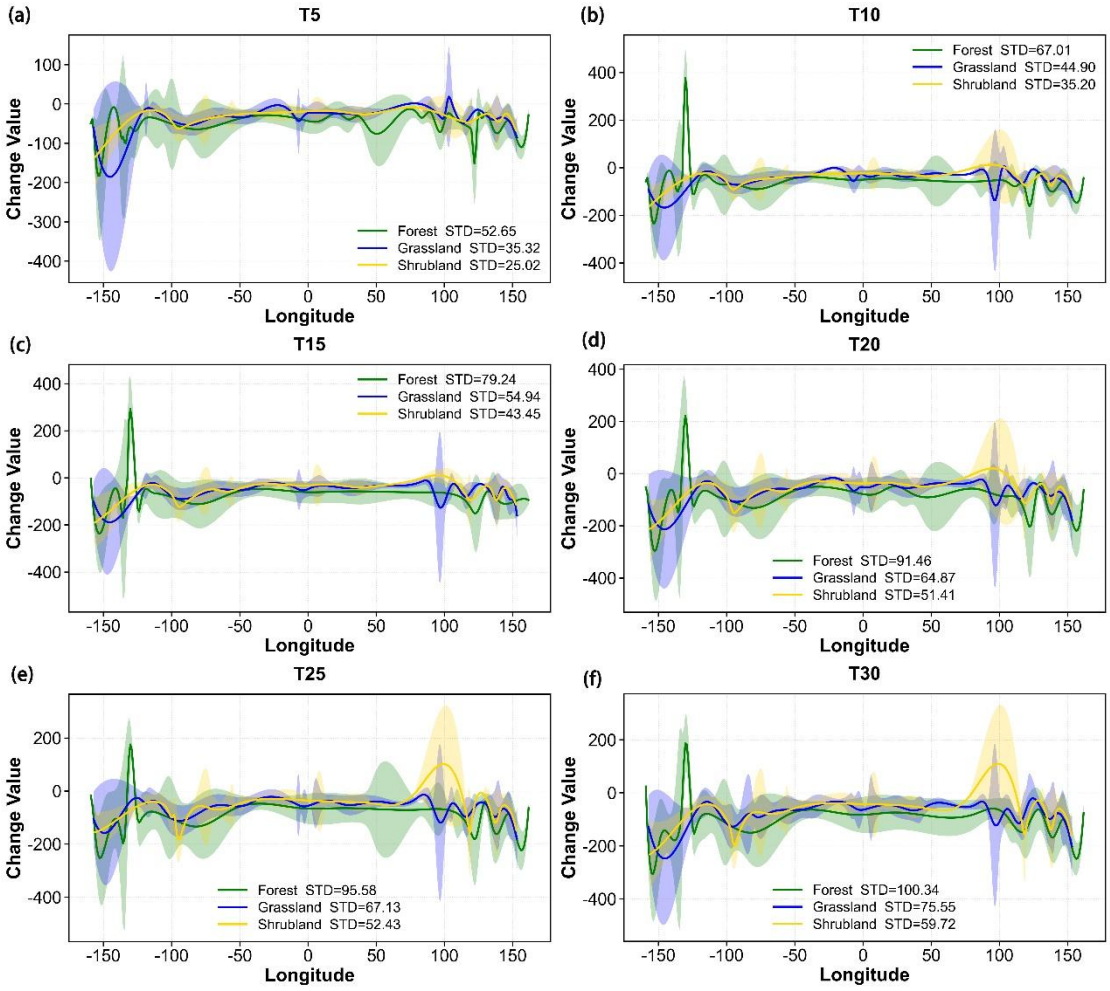


Fig. 6. Fitted profiles of point-scale ΔSOC along the longitudinal gradient for different land cover types under six warming scenarios. Panels (a)–(f) represent the T5, T10, T15, T20, T25, and T30 scenarios, respectively; curves of different colors represent forests, grasslands, and shrublands. Shaded areas with different colors indicate the standard deviation ranges of the corresponding land cover types.

As shown in Fig. S1, temperature increases gradually rise across the six scenarios. In T5 (Fig. S1(a)), temperature changes in global terrestrial non-cropland areas primarily range between 0.5 and 1.5 °C; by T15 (Fig. S1(c)), many regions have reached 2–3 °C; and by T30 (Fig. S1(f)), large areas in mid-to-high latitudes have reached 3–5 °C, with local increases exceeding 5 °C. A comparison of Fig. S1 with Figs. 5 and 6 reveals that regions with higher temperature increments are more likely to exhibit stronger negative changes in ΔSOC, particularly in mid-to-high latitude regions with concentrated forest cover. This indicates that the spatial response of SOC to warming exhibits clear regional variations, and that the negative response is stronger under high-

warming scenarios.

3.2 Accuracy Assessment and Key Driving Factors of the ΔSOC Spatial Prediction Model

Fig. 7 shows that model predictions were positively correlated with observed values across all six warming scenarios. Most data points were distributed around the 1:1 line, although deviations remained in some regions. The random forest model captured the overall spatial variation in ΔSOC, with R^2 values ranging from 0.50 to 0.54 across different warming scenarios, indicating that the model maintained relatively stable explanatory capability under different warming conditions. In terms of scatter plot distribution, the point clouds are relatively more concentrated in the T5 (Fig. 7(a)) and T10 (Fig. 7(b)) scenarios, primarily clustering near zero and in the range of moderate negative values; As the warming magnitude continues to increase, the dispersion of the scatter points along the diagonal direction increases, with more samples deviating from the 1:1 line in the ranges of large positive and large negative values; however, the majority of samples still cluster near the fitted line. Overall, the validation results across the six scenarios are consistent, indicating that the constructed ΔSOC spatial prediction model possesses good stability and cross-scenario applicability.

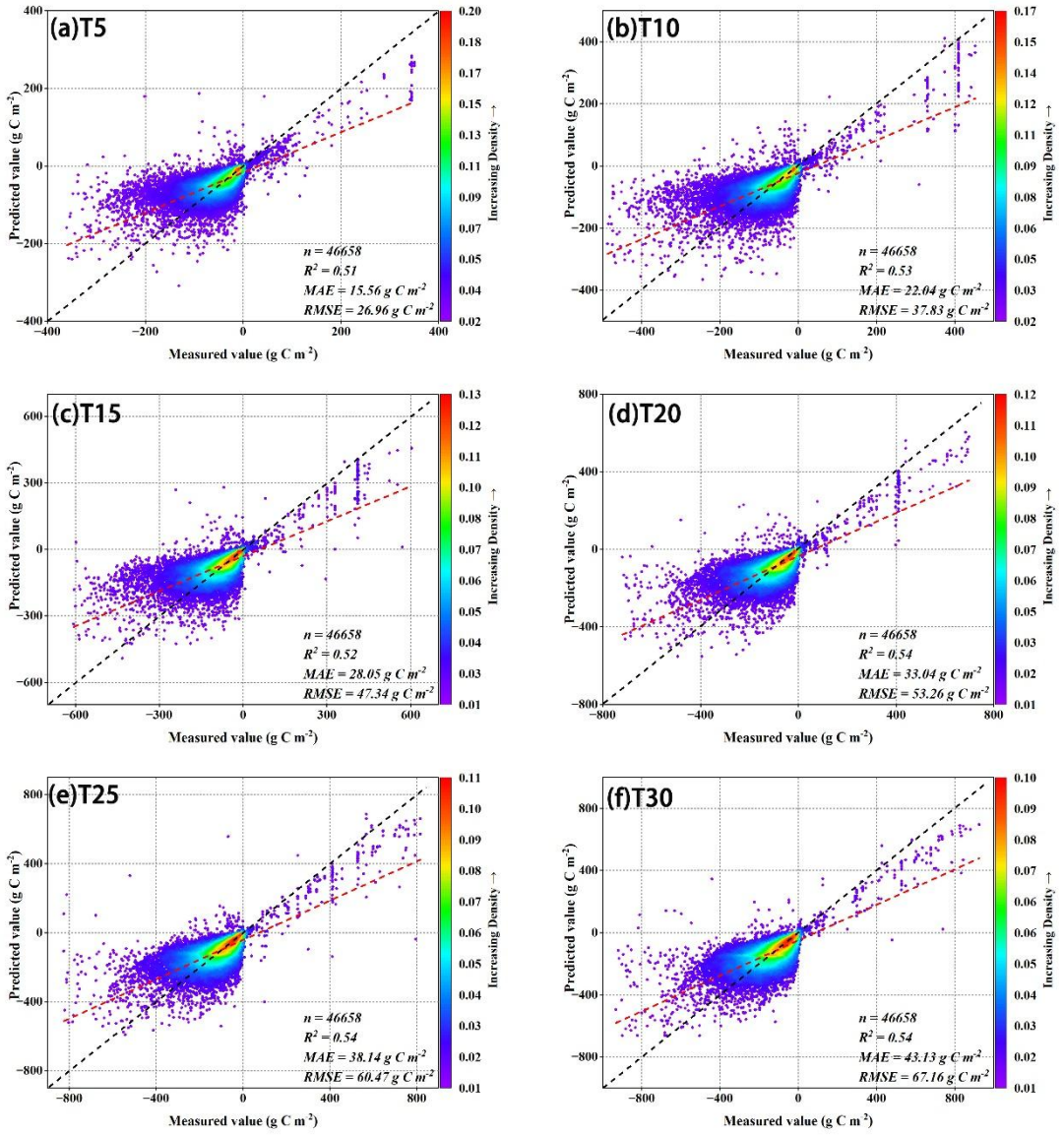


Fig. 7. Scatter plots of model accuracy across six scenarios, with accuracy metrics labeled in the lower right corner of each panel. Panels (a)–(f) represent the validation scatter plots for each scenario, respectively. The black dashed line indicates the 1:1 line, and the red dashed line indicates the fitted line.

Fig. S2 shows that the ranking of key driving factors remains generally stable across the six warming scenarios, with NPP, AMT, and CEC consistently ranking at the top. For example, under the T30 scenario, NPP, AMT, and CEC remained the three most important variables, followed by Aspect and NDVI, while Silt also showed relatively high importance. The SHAP value honeycomb plot shows that SOC content exhibits an upward trend as AMT increases and NPP decreases. The SHAP value bar ranking plot

reveals that NPP and AMT contributed more strongly to ΔSOC predictions than other variables, highlighting the roles of vegetation carbon inputs and temperature-driven processes in regulating warming-induced SOC responses. When considering all six scenarios together, although there are slight changes in the order of the top five variables, they remain primarily concentrated on NPP, AMT, CEC, Aspect, NDVI, and Silt, indicating that the dominant factors do not undergo significant replacement under different warming levels. The marginal effect curves demonstrate that the relationship between these key variables and ΔSOC is not a simple linear one. Under the T30 scenario, the response of NPP increases more rapidly in the high-value range, while AMT generally decreases with increasing temperature gradient; CEC and NDVI also exhibit largely negative trends, and the magnitude of change in Aspect is relatively small. Fig. S2 shows that this nonlinear relationship persists across all scenarios from T5 to T30, with only variations in the steepness of the curves.

Fig. 8(a) shows that the composition of driver categories across the six warming scenarios remains relatively stable overall, with no substantial shifts in their relative proportions. Across most scenarios, the dominant category accounted for approximately 35%–45%, the least important category generally accounted for 10%–20%, and the remaining categories mostly ranged between 20% and 30%. The compositional structures of forests, grasslands, and shrublands were broadly similar, indicating that the relative contributions of different driver categories were generally consistent among the three land cover types. Fig. 8(b) presents the averaged results across the six scenarios by land cover type. For forests, grasslands, and shrublands, the dominant category averaged approximately 39%, 39%, and 42%, respectively, whereas the category with the lowest proportion averaged approximately 13%, 15%, and 15%, respectively. The error bars further indicate that fluctuations in the higher-proportion categories were relatively more pronounced in forests, grasslands, and shrublands, suggesting that the driving structure of SOC responses varied to some extent among warming scenarios while maintaining a generally consistent pattern across the three land cover types.

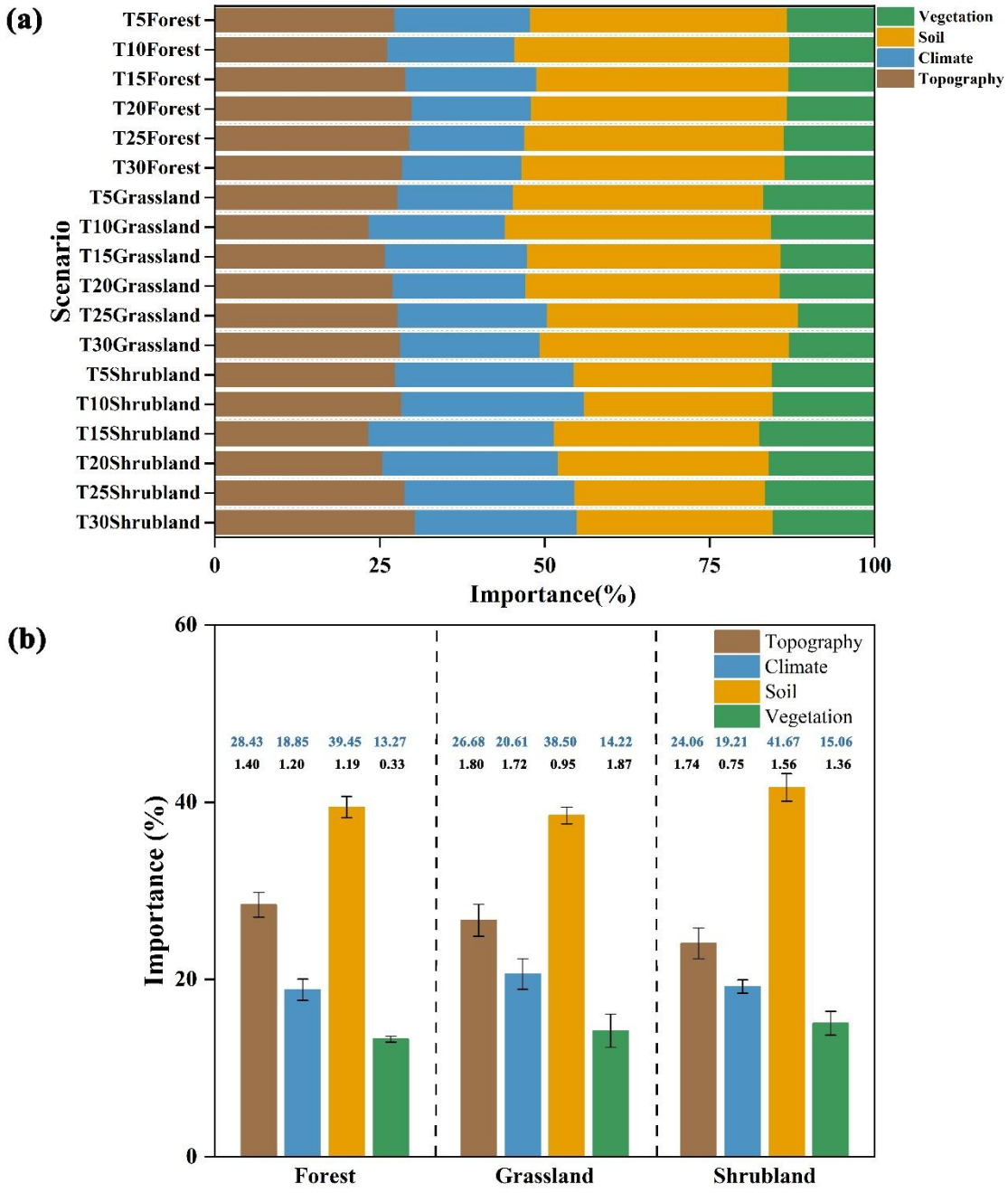


Fig. 8. Panel (a) shows the relative importance composition of the four environmental covariate groups across scenarios and land-cover types; panel (b) shows the means and standard deviations for each land-cover type across the six scenarios. Blue numbers represent the mean, and black numbers represent the standard deviation.

3.3 Spatial Distribution of SOC Response Values

Fig. S3 shows that, under constant temperature conditions, the model-predicted values maintain a good correlation with the simulated values. The scatter plot is generally distributed on both sides of the 1:1 line, and the fitted line is close to the 1:1 line;

however, there is still a certain degree of underestimation in the high-value region. The scatter plot results show an R^2 of 0.46, an MAE of 1.63 kg C m^{-2}, and an RMSE of 2.39 kg C m^{-2}, indicating that the model already possesses relatively stable fitting capabilities under the baseline scenario, which can provide a foundation for subsequent difference analyses under warming scenarios. Fig. S4 further presents the spatial distribution of SOC predictions and their uncertainties under a constant-temperature scenario. Fig. S4(a) indicates that the average SOC predictions for the 0–20 cm soil layer in global non-cropland areas exhibit significant spatial variation; high-value regions are primarily distributed in high-latitude areas of the Northern Hemisphere and some humid regions, while low-value regions are more prevalent in arid and semi-arid regions; The average value shown in the Fig. is 5.56 kg C m^{-2}. Fig. S4(b) shows that the uncertainty in SOC projections also exhibits significant spatial heterogeneity, with an average uncertainty of 0.19. Higher uncertainty is mainly concentrated in some tropical and high-latitude regions, while most regions exhibit relatively low levels.

Fig. 9 shows that the predicted ΔSOC values for the 0–20 cm soil layer in global non-cropland areas under the six warming scenarios are predominantly negative, indicating that SOC will generally decrease following warming. Spatially, negative changes are more continuous in the mid-to-high latitudes of the Northern Hemisphere, with particularly pronounced trends in northern North America and northern Eurasia. In low-latitude regions and most areas of the Southern Hemisphere, the magnitude of change is relatively small, with scattered positive changes observed in some local areas. Under the T5–T30 scenarios, the mean ΔSOC values range from −40.23 to −92.73 g C m^{-2}, while the median ranges from −38.76 to −86.65 g C m^{-2}. All six scenarios yield negative values, with T30 showing the largest decrease. The proportion of area under negative values is concentrated across all scenarios and increases with rising temperatures, with the proportion of areas experiencing stronger negative changes growing, indicating that the extent and intensity of SOC loss further expand under high-warming scenarios.

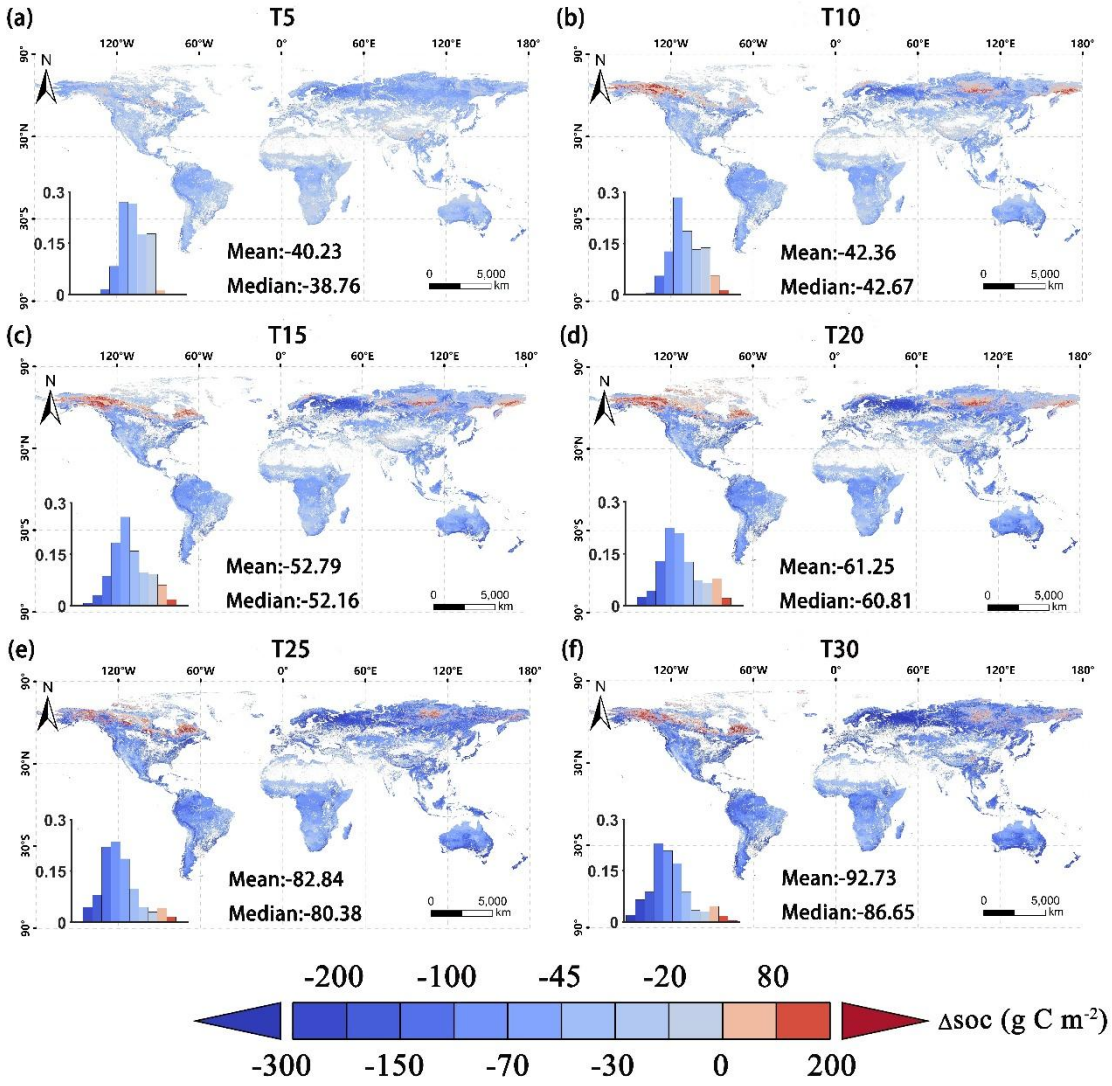


Fig. 9. Spatial distribution of predicted ΔSOC (g C m^{-2}) in the 0 – 20 cm soil layer of global terrestrial non-cropland areas after a one-year simulation under six temperature-perturbation scenarios. The inset in the lower-left corner shows the area proportions of different ΔSOC classes.

Fig. 10 shows that the uncertainty in ΔSOC projections exhibits significant spatial heterogeneity across the six warming scenarios. High-value regions are primarily concentrated in the mid-to-high latitudes of the Northern Hemisphere, with particularly continuous patterns observed in northern North America and northern Eurasia, while low-value regions are mostly distributed in low-latitude areas and parts of the Southern Hemisphere. This spatial pattern is generally consistent across different scenarios, but regions of high uncertainty are more pronounced under high-warming scenarios. The mean uncertainty values are high across all scenarios: 0.47, 0.74, 0.85, and 0.78 for the

T5 (Fig. 10(a)), T15 (Fig. 10(c)), T25 (Fig. 10(e)), and T30 (Fig. 10(f)) scenarios, respectively. While T10 (Fig. 10(b)) and T20 (Fig. 10(d)) are both around 0.5. The medians are lower than the corresponding means, indicating a right-skewed distribution of uncertainty, with a few high-value regions contributing significantly to the overall mean. Combined with the bar charts, it can be seen that most regions remain concentrated in the low-to-medium uncertainty range, while the high-uncertainty range covers a relatively small area.

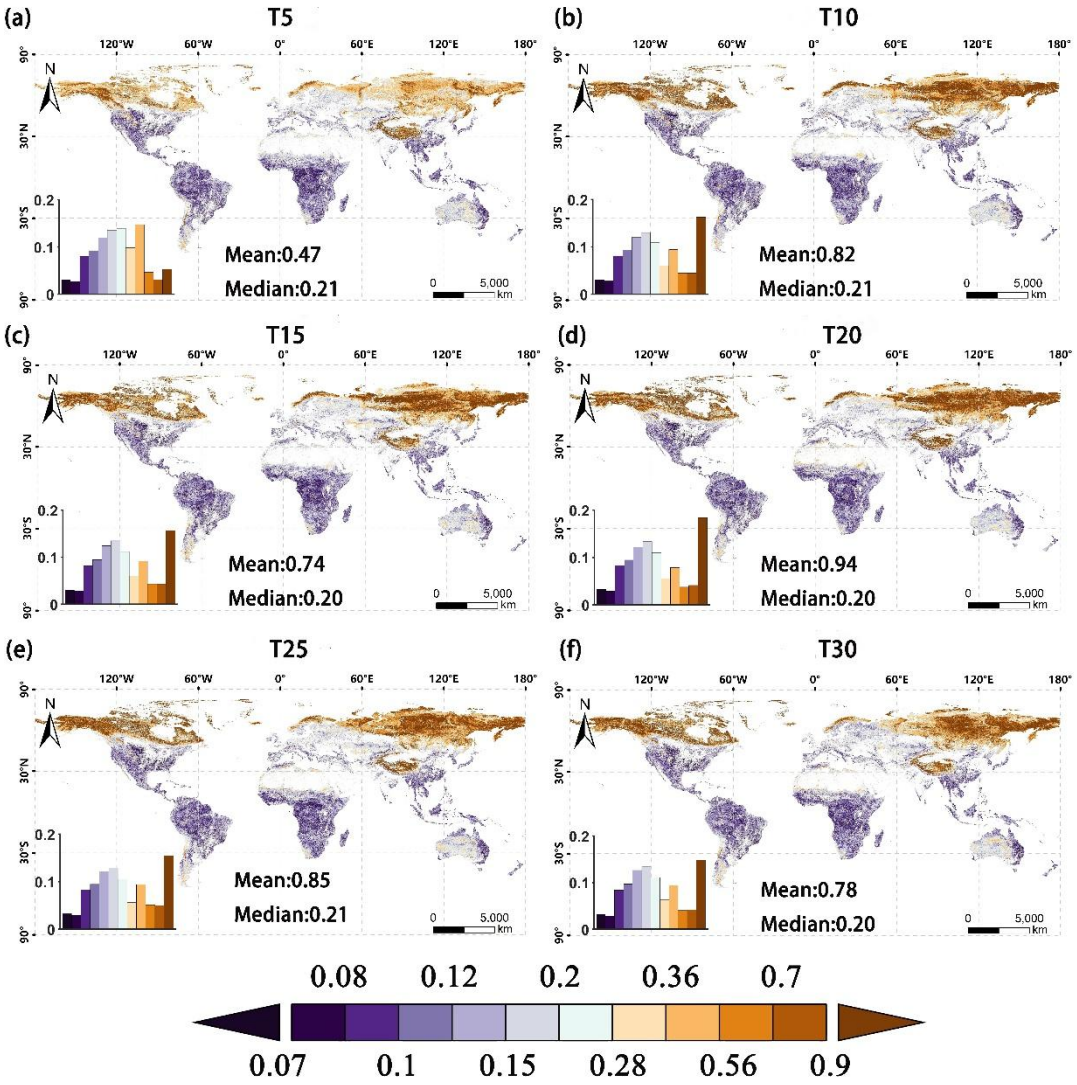


Fig. 10. ΔSOC uncertainty values at the 0–20 cm depth in global terrestrial non-cropland areas under six scenarios. The inset in the lower left corner shows the area proportions for different ΔSOC levels

In Fig. S5, changes in SOC stocks in the 0–20 cm soil layer of global non-cropland areas under the six warming scenarios are all negative, indicating that SOC stocks

generally decrease across all scenarios, with the magnitude of the decrease gradually increasing as warming intensifies. The changes in SOC stocks under the T5, T10, T15, T20, T25, and T30 scenarios are −7.58, −8.04, −10.02, −11.63, −15.72, and −17.60 Pg, respectively. The rate of decline increased relatively gradually from the T5 to T20 scenarios, but accelerated further beyond T20, with the T30 scenario showing the greatest SOC loss. The standard deviations for the six scenarios were 0.64, 1.01, 1.23, 1.48, 2.04, and 1.99 Pg, respectively, and generally increased with rising temperatures. This indicates that under high-warming scenarios, not only is SOC loss greater, but the variability within the scenarios is also higher.

Fig. 11 shows that SOC changes in the 0–20 cm soil layer across the three land cover types were negative under all six warming scenarios, and generally continued to decline as warming intensified. The forest land cover (Fig. 11(a)) exhibited the largest SOC reduction, decreasing gradually from −5.13 Pg at T5 to −11.88 Pg at T30, with the standard deviation also increasing from 0.41 Pg to 1.26 Pg. The grassland land cover type (Fig. 11(b)) followed, with SOC changes decreasing from −1.80 Pg to −4.13 Pg, and the standard deviation increasing from 0.18 Pg to 0.59 Pg. The change in the shrubland land cover type (Fig. 11(c)) was relatively small but also showed a continuous downward trend, with the SOC change decreasing from −0.63 Pg to −1.54 Pg and the standard deviation increasing from 0.05 Pg to 0.14 Pg. There are significant differences in the intensity of warming responses among land cover types, with forests showing the greatest response, followed by grasslands and shrublands.

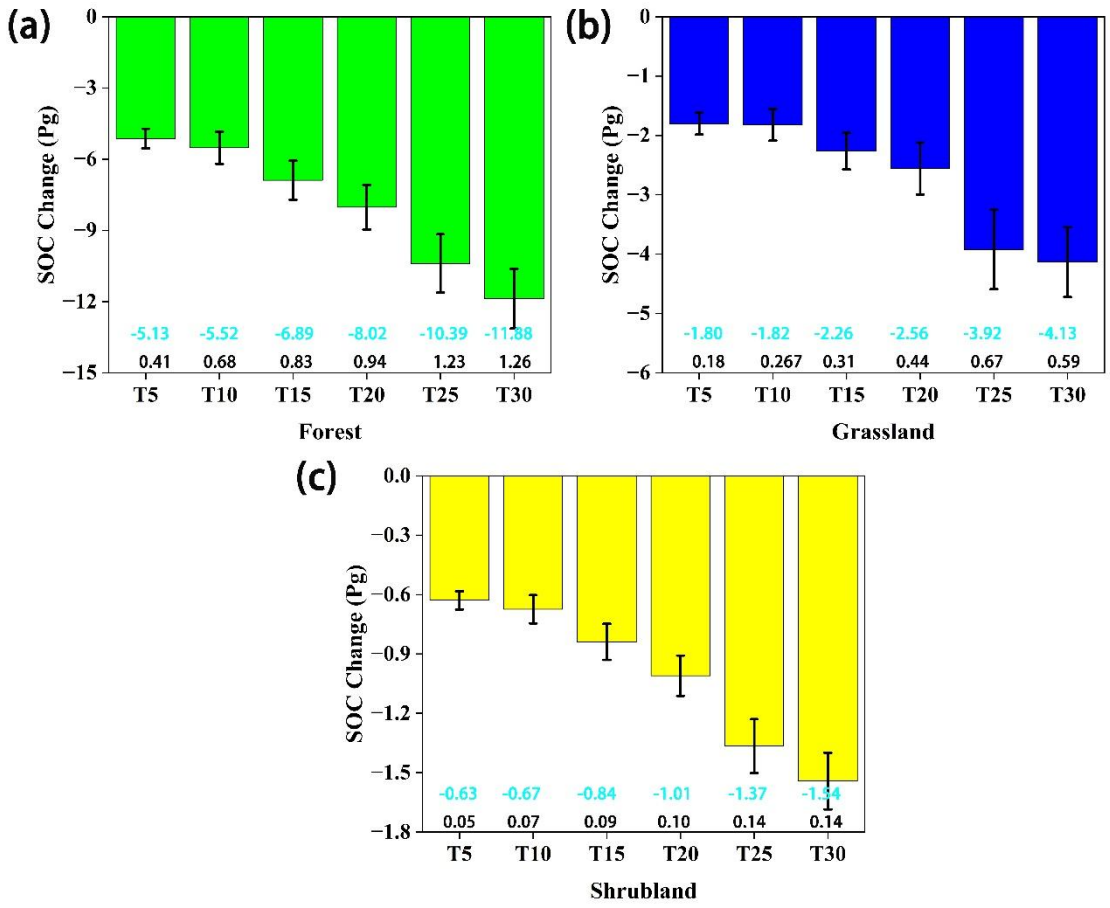


Fig. 11. Changes in ΔSOC in the 0–20 cm layer for different land cover types under six scenarios: (a) represents forest, (b) represents grassland, and (c) represents shrubland. Error bars indicate standard deviation. The blue numbers below the bars indicate the specific reduction amounts for each land cover type under different warming scenarios, and the black numbers below indicate the standard deviation.

Fig. 12 shows that ΔSOC is negative across all climate zones under the six warming scenarios, but the magnitude of the decrease varies significantly. The continental climate zone (Fig. 12(d)) consistently shows the strongest response, with SOC changes decreasing from −3.53 Pg at T5 to −7.69 Pg at T30, and the corresponding standard deviation increasing from 0.41 Pg to 1.36 Pg, which is significantly higher than in other climate zones. The tropical (Fig. 12(a)) and temperate (Fig. 12(c)) climate zones were at intermediate levels, with the tropical zone decreasing from −1.46 Pg to −3.26 Pg and the temperate zone from −1.38 Pg to −3.83 Pg; the standard deviations for both increased as the scenario progressed. Changes in the arid climate zone (Fig. 12(b)) were relatively weak, with ΔSOC decreasing from −0.78 Pg to −2.16 Pg. The

polar climate zone (Fig. 12(e)) remained the lowest, fluctuating only between −0.27 and −0.67 Pg across the six scenarios. Overall, as warming intensified, SOC losses continued to increase in most climate zones, with only minor fluctuations observed between certain adjacent scenarios in the continental and polar climate zones.

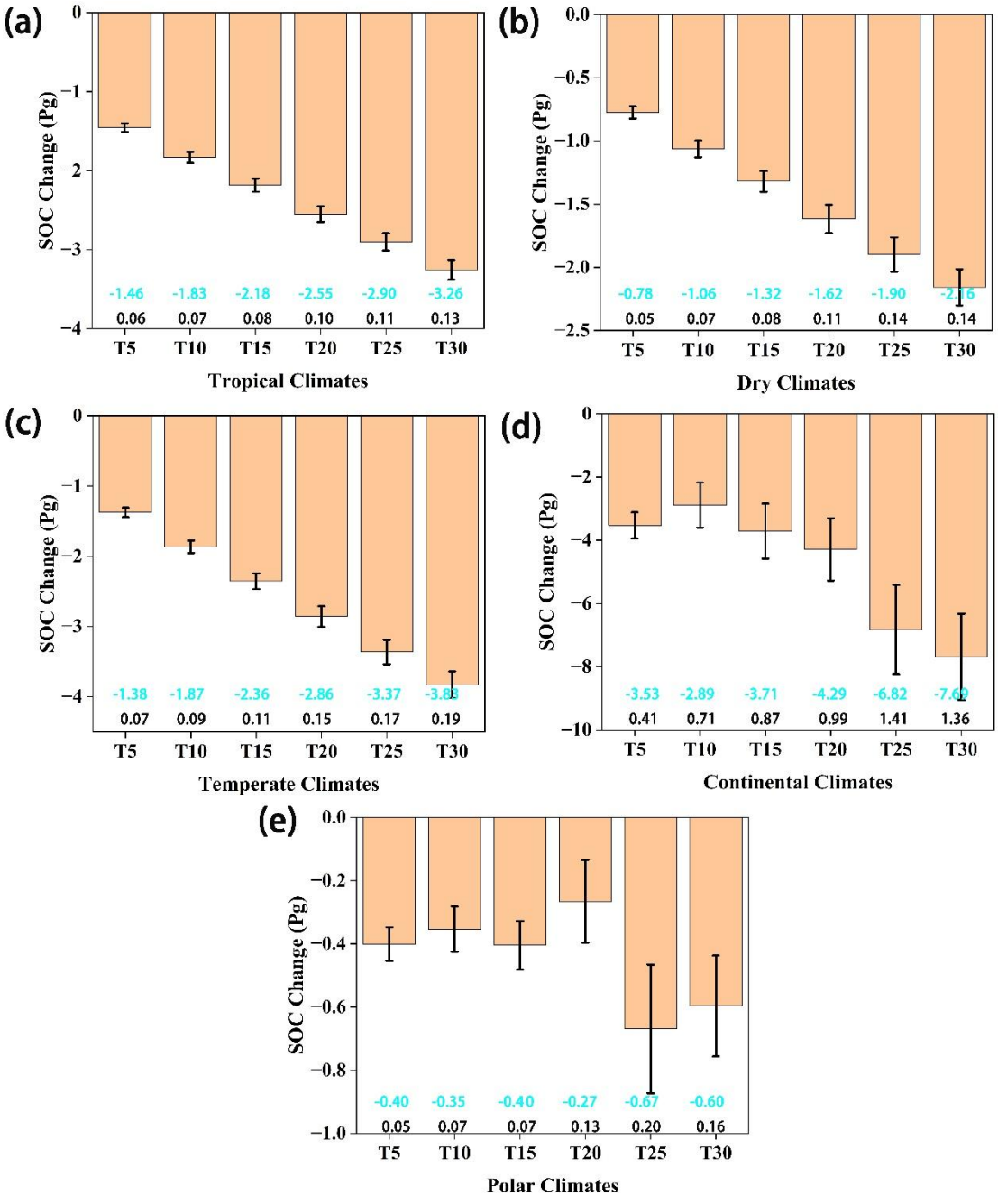


Fig. 12. Changes in Δ SOC in the 0–20 cm layer across different climates under six scenarios: (a) represents tropical climate, (b) represents arid climate, (c) represents temperate climate, (d) represents continental climate, and (e) represents the polar climate. Error bars represent standard deviation. The blue numbers below the bars for each climate zone

correspond to the specific reduction amounts, while the black numbers below correspond to the standard deviation.

3.4 Comparison and Validation of SOC Stock Changes with Other Studies

The ΔSOC values simulated in this study under various temperature increase scenarios were compared with existing warming experiment results (Bouskill et al., 2014; Chen et al., 2020; Cheng et al., 2017; Crowther et al., 2016; Lu et al., 2013; Xu and Yuan, 2017; Yan et al., 2020). As shown in Fig. 13, both sets of results indicate that the rate of SOC change decreases with increasing temperature, suggesting that soil organic carbon loss will generally intensify under enhanced warming conditions. In this study, the rate of SOC change exhibits a relatively steady decline along the temperature gradient, decreasing gradually from approximately −2% to close to −4%. In contrast, the warming experiments exhibited greater variability, with results ranging from near-zero or slightly above zero to stronger negative changes within the moderate warming range, showing a more pronounced decline around 4–5 °C, with the lowest value approaching −10%. Fluctuations in the warming experiments were generally larger across temperature intervals than in this study, while the error range in this study was relatively smaller, indicating that the simulation results are more stable at different temperature levels. The sample sizes shown in the Fig. also indicate that the number of observed warming experiments in the high-temperature range is relatively small; the number of labeled samples decreases from 73 and 106 in the low-temperature range to 10 and 6 in the high-temperature range, resulting in higher uncertainty in experimental results under high-temperature conditions. Overall, this study is consistent with existing warming experiments in terms of the direction of change, but the temperature response curves presented here are more continuous and exhibit lower variability.

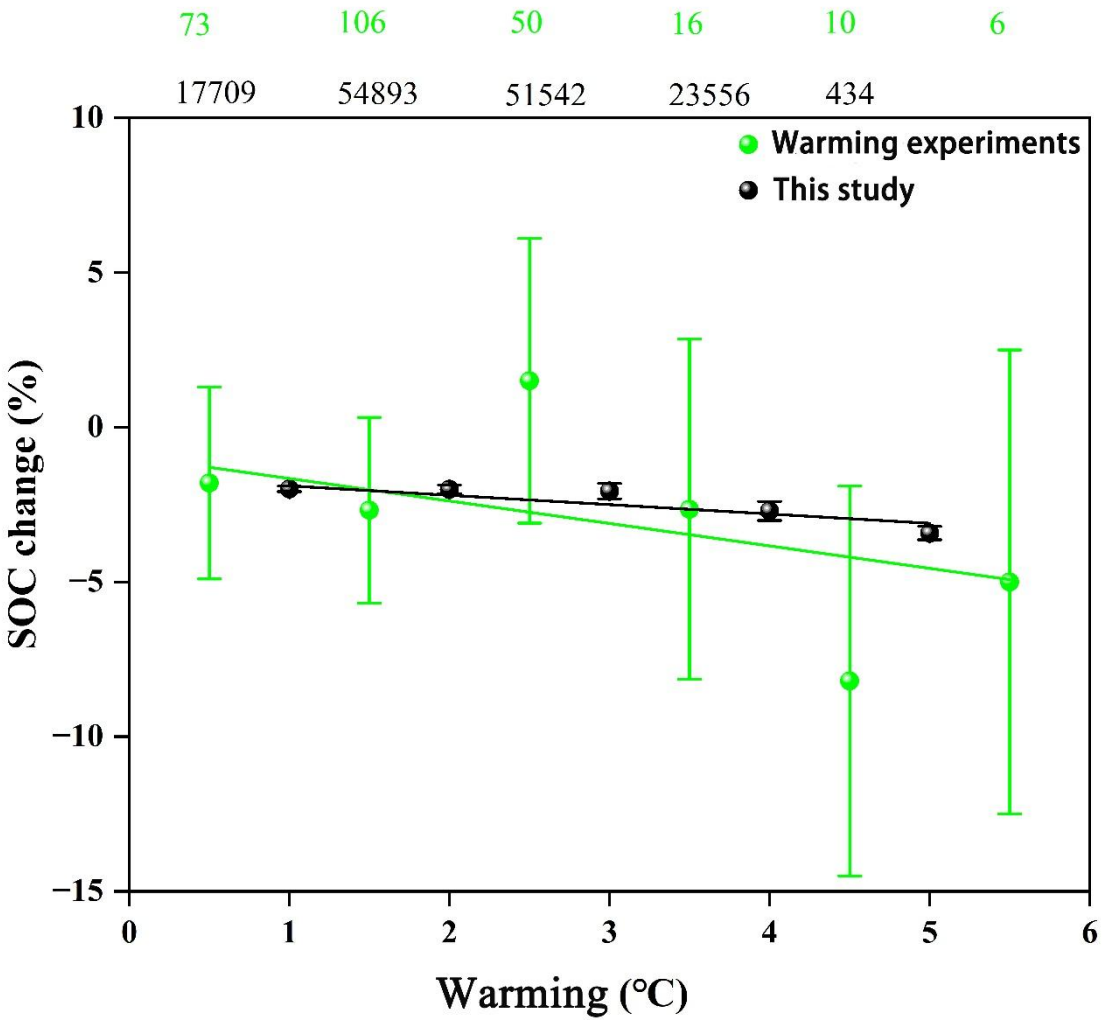


Fig. 13. Comparison of the results from this study at various temperatures with those from other warming experiments; error bars represent standard deviation, and the numbers indicate the sample size used in each experiment.

4. Discussion

The results of this study (Figs. 3–4, Fig. S1) show that, under the six warming scenarios, the global ΔSOC in the 0–20 cm soil layer of non-cropland is predominantly negative. As the magnitude of warming increases, SOC losses continue to deepen, with the strongest decline in forests, followed by grasslands and shrublands. Results from latitudinal and longitudinal profiles (Figs. 5 – 6) also indicate that the negative response of ΔSOC is not uniformly distributed globally. Instead, stronger fluctuations and losses are observed in the mid-to-high latitudes of the Northern Hemisphere, the mid-latitudes of the Southern Hemisphere, and certain longitudinal zones. This suggests that the point-scale response of SOC to warming exhibits both significant land cover differences

and geographical gradient variations. This indicates that under conditions where only temperature is altered, climate warming generally enhances soil organic carbon loss, and there are significant differences in sensitivity to warming across different land cover types and latitudinal and longitudinal regions. These results are consistent with existing research conclusions regarding the promotion of SOC decomposition and carbon release by warming (Crowther et al., 2016; Davidson and Janssens, 2006; Melillo et al., 2017). A possible explanation is that warming enhances microbial activity and the rate of organic matter mineralization, there by promoting the turnover of the active carbon pool; meanwhile, forest soils have relatively high carbon inputs and proportions of active organic matter, making them more sensitive to temperature disturbances (Coleman and Jenkinson, 1996; Tang et al., 2017). In contrast, increases in SOC observed at some sites in grasslands and shrublands may be related to enhanced plant productivity and root carbon input under warming conditions, which partially offset decomposition losses (Bai and Cotrufo, 2022; Liu et al., 2021; Yan et al., 2022).

The results also show (Fig. 7, Fig. S2) that the validation accuracy of the random forest model remained relatively stable across the six warming scenarios, with R^2 values ranging from 0.50 to 0.54, and the ranking of key driving factors was largely consistent, with NPP, AMT, and CEC consistently ranking among the most important predictors. This indicates that the RothC-RF coupling framework captured relatively consistent spatial patterns of ΔSOC under different warming scenarios, and the relative importance of the major controlling processes remained stable across warming gradients. This consistency may be attributed to the complementary roles of vegetation carbon inputs, temperature-driven decomposition, and soil carbon stabilization processes in regulating SOC responses to warming (Zhang et al., 2024). NPP primarily represents ecosystem carbon input capacity, which determines the extent to which vegetation-derived carbon inputs can compensate for warming-enhanced decomposition. Previous studies have demonstrated that changes in primary productivity and carbon allocation strongly influence soil carbon accumulation by regulating carbon inputs into terrestrial ecosystems. In contrast, AMT regulates SOC turnover by influencing temperature-dependent decomposition processes, as higher

temperatures generally accelerate microbial activity and organic matter decomposition, thereby increasing carbon losses from soil pools. Meanwhile, CEC reflects soil mineral protection capacity and contributes to the stabilization and persistence of organic carbon by regulating interactions between organic matter and mineral surfaces (Doetterl et al., 2015; Hemingway et al., 2019; Torn et al., 1997). Therefore, warming-induced SOC responses are not controlled by a single environmental factor but emerge from the balance between carbon inputs, decomposition losses, and soil carbon stabilization processes. The consistent contribution of these factors across warming scenarios suggests that the fundamental ecological processes regulating SOC responses remain relatively stable under different warming intensities.

Spatial results (Fig. 9) further show that the negative response of SOC is primarily concentrated in the mid-to-high latitudes of the Northern Hemisphere, with its extent and intensity increasing under high warming scenarios; across different climate zones (Fig. 12), losses are most severe in continental climate zones, forest land types (Fig. 11) are most sensitive to warming, and uncertainty (Fig. 10) is relatively higher in high-latitude and some arid regions. This indicates that the response of SOC to climate warming exhibits significant spatial heterogeneity, with background hydrometeorological conditions, vegetation types, and data availability in different regions all influencing the prediction results. These findings are consistent with existing research conclusions regarding marked regional differences in soil carbon feedbacks (Bradford et al., 2016; Schuur et al., 2015). Possible reasons for this include the fact that in warm and humid regions, warming tends to further intensify microbial respiration and organic matter mineralization, whereas in cold regions, although warming may promote a longer growing season and increased carbon input, this compensatory effect is insufficient to fully offset SOC losses on a global scale; simultaneously, the relatively sparse sampling in high-latitude regions also amplifies the uncertainty of spatial predictions (Hengl et al., 2017).

A comparison with results from independent warming experiments (Fig. 13) shows that the SOC changes simulated in this study decrease as temperature rises, consistent with the general trend observed in previous studies; however, the temperature response

curve in this study is smoother and exhibits lower variability. This indicates that the process-data fusion framework effectively captures the overall response pattern of global-scale SOC to warming. These results are consistent with findings from studies showing a sustained decline in SOC under global warming conditions across biogeographic regions (Wang et al., 2024). This may be attributed to the fact that global-scale simulations spatially average local extreme responses, while uniform scenario settings and fixed non-temperature factors reduce the amplitude of fluctuations between different regions, resulting in model outcomes that are more continuous and stable than those from in situ warming experiments.

The significance of this study also lies in its focus on global terrestrial non-cropland ecosystems, whereas existing SOC simulation studies have primarily concentrated on areas with strong anthropogenic disturbances, such as croplands (Dechow et al., 2019; Giltrap et al., 2010; Smith et al., 2007; Wang et al., 2022). The results show (Fig. S5) that SOC in terrestrial non-cropland areas generally decreases under warming scenarios, with the rate of decline accelerating under high-warming scenarios. This suggests that continued warming could increase the vulnerability of terrestrial non-cropland soil carbon pools to carbon loss under future warming scenarios. This finding is consistent with discussions regarding the uncertainty of soil carbon feedbacks and their climate implications (Bradford et al., 2016).

In addition to the findings described above, this study has several limitations. This study focused on the isolated effects of warming by modifying temperature while keeping other environmental factors constant. Although this approach enables a direct assessment of temperature impacts on SOC dynamics, future climate change involves simultaneous variations in precipitation, atmospheric CO_2 concentration, and vegetation conditions, which may further regulate SOC responses. Another source of uncertainty arises from the estimation of carbon inputs, environmental covariates, and model parameterization. In particular, the NPP scaling method used in this study may not fully capture differences in litter production and fine-root turnover among ecosystems (Gottschalk et al., 2012; Hengl et al., 2017; Smith et al., 2005). Furthermore, while RothC effectively represents major SOC turnover processes, some complex

mechanisms, including microbial adaptation, priming effects, and mineral-associated organic carbon dynamics, are not explicitly considered. Future studies integrating more comprehensive climate scenarios, higher-resolution data, and long-term observations will help further improve the simulation of SOC responses to global warming.

Conclusion

Based on a coupled framework of the RothC process model and a random forest model, this study systematically assessed the response characteristics of SOC in global terrestrial non-cropland areas to multi-gradient warming scenarios. The results indicate that this framework can effectively capture the spatial patterns of simulated SOC responses to warming, with a coefficient of determination ranging from 0.50 to 0.54 in the model validation under warming scenarios. SOC in the 0–20 cm soil layer across global terrestrial non-cropland areas exhibits net losses under all warming scenarios, with the magnitude of these losses increasing continuously as warming intensifies: from the T5 to T30 scenarios, global SOC stocks decrease by 7.58–17.60 Pg, corresponding to an average ΔSOC of −40.23 to −92.73 g C m^{-2}. The SOC response exhibits significant spatial heterogeneity, with areas of high loss primarily concentrated in mid-to-high latitude and high-altitude regions such as northern North America, northern Eurasia, and the periphery of the Tibetan Plateau. Responses vary markedly across different climate zones and land cover types, with continental climate zones and forest land cover contributing the largest SOC losses; under the T30 scenario, SOC in forest land cover decreases by as much as 11.88 Pg. Driving factor analysis indicates stable yet non-linear controlling relationships across different scenarios, with NPP and annual mean temperature emerging as the dominant single predictors; meanwhile, soil and topographic factors jointly contribute the greatest explanatory power across various land cover types. However, high-latitude regions, arid zones, and environmental transition zones exhibit higher uncertainty. The climate scenario–SOC response simulation framework proposed in this study can effectively support global non-cropland carbon cycle assessments, providing a methodological reference for regional carbon assessment and future studies on SOC–climate feedbacks under climate change,

while also revealing an accelerating trend in SOC loss under strong warming scenarios.

Abbreviations

profile curvature	PRC
Elevation	Elev
Annual mean precipitation	AMP
Annual mean temperature	AMT
Annual mean potential evapotranspiration	AME
Cation exchange capacity	CEC
Silt content	Silt
Soil pH in H_2O	Phh2o
Bulk Density of the fine earth fraction	BD
Coarse Fragments Volumetric fraction	CFVO
Normalized difference vegetation index	NDVI
Net primary production	NPP

Declarations

Ethics approval and consent to participate

Not applicable.

Consent for publication

Not applicable.

Data availability

The datasets used in this study are available from publicly accessible sources. The corresponding author can provide additional information regarding data processing and integration upon reasonable request.

Competing interests

The authors declare that they have no known competing financial interests or personal relationships that could have appeared to influence the work reported in this paper.

Funding

This study was supported by the National Natural Science Foundation of China (Nos. 42501070 and 42501071), the Natural Science Foundation of Xinjiang Uygur Autonomous Region (No. 2025D01C27), and the talent program “Tianchi Talent (Young Doctor)” of the Xinjiang Uygur Autonomous Region.

Author contributions

KQW handled conceptualization, data curation, formal analysis, validation, and manuscript drafting. **ZPZ** contributed to manuscript review and editing, validation, visualization, funding acquisition, and project administration. **XYG** provided resources and supervision. **LJH** contributed to investigation, methodology, and resources. **JZW** contributed to investigation, methodology, and resources. **JLD** was responsible for project administration. **LZ** contributed to manuscript review and editing. All authors read and approved the final manuscript.

Acknowledgments

We gratefully acknowledge Xinjiang University for providing the platform and support. We would like to express our gratitude to the editor and anonymous reviewers for their insightful comments and suggestions.

References

Bai, Y., Cotrufo, M.F., 2022. Grassland soil carbon sequestration: Current understanding, challenges, and solutions. Science 377(6606), 603-608. https://doi.org/10.1126/science.abo2380

Batjes, N.H., 2014. Total carbon and nitrogen in the soils of the world. European Journal of Soil Science 65(1), 10-21. https://doi.org/10.1111/ejss.12114_2

Batjes, N.H., Ribeiro, E., van Oostrum, A., 2020. Standardised soil profile data to support global mapping and modelling (WoSIS snapshot 2019). Earth Syst. Sci. Data 12(1), 299-320. https://doi.org/10.5194/essd-12-299-2020

Bernardini, L.G., Rosinger, C., Bodner, G., Keiblinger, K.M., Izquierdo-Verdiguier, E., Spiegel, H., Retzlaff, C.O., Holzinger, A., 2024. Learning vs. understanding: When does artificial intelligence outperform process-based modeling in soil organic carbon prediction? New Biotechnology 81, 20-31. https://doi.org/10.1016/j.nbt.2024.03.001

Bouskill, N.J., Riley, W.J., Tang, J.Y., 2014. Meta-analysis of high-latitude nitrogen-addition and warming studies implies ecological mechanisms overlooked by land models.

Biogeosciences 11(23), 6969-6983. https://doi.org/10.5194/bg-11-6969-2014
Bradford, M.A., Wieder, W.R., Bonan, G.B., Fierer, N., Raymond, P.A., Crowther, T.W., 2016. Managing uncertainty in soil carbon feedbacks to climate change. Nature Climate Change 6(8), 751–758. https://doi.org/10.1038/nclimate3071
Breiman, L., 2001. Random forests. Machine Learning 45(1), 5–32. https://doi.org/10.1023/A:1010933404324
Chen, Y., Feng, J., Yuan, X., Zhu, B., 2020. Effects of warming on carbon and nitrogen cycling in alpine grassland ecosystems on the Tibetan Plateau: A meta-analysis. Geoderma 370, 114363. https://doi.org/10.1016/j.geoderma.2020.114363
Cheng, L., Zhang, N., Yuan, M., Xiao, J., Qin, Y., Deng, Y., Tu, Q., Xue, K., Van Nostrand, J.D., Wu, L., He, Z., Zhou, X., Leigh, M.B., Konstantinidis, K.T., Schuur, E.A.G., Luo, Y., Tiedje, J.M., Zhou, J., 2017. Warming enhances old organic carbon decomposition through altering functional microbial communities. The ISME Journal 11(8), 1825-1835. https://doi.org/10.1038/ismej.2017.48
Coleman, K., Jenkinson, D.S., 1996. RothC-26.3 - A Model for the turnover of carbon in soil. In: D.S. Powlson, P. Smith, J.U. Smith (Eds.), Evaluation of Soil Organic Matter Models. Springer Berlin Heidelberg, Berlin, Heidelberg, pp. 237–246.
Craney, T.A., Surles, J.G., 2002. Model-Dependent Variance Inflation Factor Cutoff Values. Quality Engineering 14(3), 391-403. https://doi.org/10.1081/QEN-120001878
Crowther, T.W., Todd-Brown, K.E.O., Rowe, C.W., Wieder, W.R., Carey, J.C., Machmuller, M.B., Snoek, B.L., Fang, S., Zhou, G., Allison, S.D., Blair, J.M., Bridgham, S.D., Burton, A.J., Carrillo, Y., Reich, P.B., Clark, J.S., Classen, A.T., Dijkstra, F.A., Elberling, B., Emmett, B.A., Estiarte, M., Frey, S.D., Guo, J., Harte, J., Jiang, L., Johnson, B.R., Kröel-Dulay, G., Larsen, K.S., Laudon, H., Lavallee, J.M., Luo, Y., Lupascu, M., Ma, L.N., Marhan, S., Michelsen, A., Mohan, J., Niu, S., Pendall, E., Peñuelas, J., Pfeifer-Meister, L., Poll, C., Reinsch, S., Reynolds, L.L., Schmidt, I.K., Sistla, S., Sokol, N.W., Templer, P.H., Treseder, K.K., Welker, J.M., Bradford, M.A., 2016. Quantifying global soil carbon losses in response to warming. Nature 540(7631), 104-108. https://doi.org/10.1038/nature20150
Davidson, E.A., Janssens, I.A., 2006. Temperature sensitivity of soil carbon decomposition and feedbacks to climate change. Nature 440(7081), 165-173. https://doi.org/10.1038/nature04514
Dechow, R., Franko, U., Kätterer, T., Kolbe, H., 2019. Evaluation of the RothC model as a prognostic tool for the prediction of SOC trends in response to management practices on arable land. Geoderma 337, 463-478. https://doi.org/10.1016/j.geoderma.2018.10.001
Doetterl, S., Stevens, A., Six, J., Merckx, R., Van Oost, K., Casanova Pinto, M., Casanova-Katny, A., Muñoz, C., Boudin, M., Zagal Venegas, E., Boeckx, P., 2015. Soil carbon storage controlled by interactions between geochemistry and climate. Nature Geoscience 8(10), 780-783. https://doi.org/10.1038/ngeo2516
Falloon, P., Smith, P., Coleman, K., Marshall, S., 1998. Estimating the size of the inert organic matter pool from total soil organic carbon content for use in the Rothamsted carbon model. Soil Biology and Biochemistry 30(8), 1207-1211. https://doi.org/10.1016/S0038-0717(97)00256-3

FAO, 2025. Land statistics 2001–2023. Global, regional and country trends. FAOSTAT Analytical Brief No. 107. Food and Agriculture Organization of the United Nations, Rome. https://doi.org/10.4060/cd5765en

Friedman, J.H., 2001. Greedy function approximation: A gradient boosting machine. The Annals of Statistics 29(5), 1189–1232.

Giltrap, D.L., Li, C., Saggar, S., 2010. DNDC: A process-based model of greenhouse gas fluxes from agricultural soils. Agriculture, Ecosystems & Environment 136(3), 292-300. https://doi.org/10.1016/j.agee.2009.06.014

Goldstein, A., Kapelner, A., Bleich, J., Pitkin, E., 2015. Peeking Inside the Black Box: Visualizing Statistical Learning With Plots of Individual Conditional Expectation. Journal of Computational and Graphical Statistics 24(1), 44-65. https://doi.org/10.1080/10618600.2014.907095

Gottschalk, P., Smith, J.U., Wattenbach, M., Bellarby, J., Stehfest, E., Arnell, N., Osborn, T.J., Jones, C., Smith, P., 2012. How will organic carbon stocks in mineral soils evolve under future climate? Global projections using RothC for a range of climate change scenarios. Biogeosciences 9(8), 3151-3171. https://doi.org/10.5194/bg-9-3151-2012

Hemingway, J.D., Rothman, D.H., Grant, K.E., Rosengard, S.Z., Eglinton, T.I., Derry, L.A., Galy, V.V., 2019. Mineral protection regulates long-term global preservation of natural organic carbon. Nature 570(7760), 228-231. https://doi.org/10.1038/s41586-019-1280-6

Hengl, T., Mendes de Jesus, J., Heuvelink, G.B.M., Ruiperez Gonzalez, M., Kilibarda, M., Blagotić, A., Shangguan, W., Wright, M.N., Geng, X., Bauer-Marschallinger, B., Guevara, M.A., Vargas, R., MacMillan, R.A., Batjes, N.H., Leenaars, J.G.B., Ribeiro, E., Wheeler, I., Mantel, S., Kempen, B., 2017. SoilGrids250m: Global gridded soil information based on machine learning. PLOS ONE 12(2), e0169748. https://doi.org/10.1371/journal.pone.0169748

JPL, 2013. NASA Shuttle Radar Topography Mission Global 1 arc second. NASA Land Processes Distributed Active Archive Center. https://doi.org/10.5067/MEASURES/SRTM/SRTMGL1.003

Karhu, K., Gärdenäs, A.I., Heikkinen, J., Vanhala, P., Tuomi, M., Liski, J., 2012. Impacts of organic amendments on carbon stocks of an agricultural soil — Comparison of model-simulations to measurements. Geoderma 189-190, 606-616. https://doi.org/10.1016/j.geoderma.2012.06.007

Kasraei, B., Schmidt, M.G., Zhang, J., Bulmer, C.E., Filatow, D.S., Arbor, A., Pennell, T., Heung, B., 2024. A framework for optimizing environmental covariates to support model interpretability in digital soil mapping. Geoderma 445, 116873. https://doi.org/10.1016/j.geoderma.2024.116873

Lamichhane, S., Kumar, L., Wilson, B., 2019. Digital soil mapping algorithms and covariates for soil organic carbon mapping and their implications: A review. Geoderma 352, 395-413. https://doi.org/10.1016/j.geoderma.2019.05.031

Liu, M., Wen, J.-H., Chen, Y.-M., Xu, W.-J., Wang, Q., Ma, Z.-L., 2021. Warming increases soil carbon input in a Sibiraea angustata-dominated alpine shrub ecosystem. Journal of Plant Ecology 15(2), 335-346. https://doi.org/10.1093/jpe/rtab101

Louppe, G., Wehenkel, L., Sutera, A., Geurts, P., 2013. Understanding variable importances in Forests of randomized trees, 26.

Lu, M., Zhou, X., Yang, Q., Li, H., Luo, Y., Fang, C., Chen, J., Yang, X., Li, B., 2013. Responses of ecosystem carbon cycle to experimental warming: a meta-analysis. Ecology 94(3), 726-738. https://doi.org/10.1890/12-0279.1

Lundberg, S.M., Lee, S.-I., 2017. A unified approach to interpreting model predictions, Proceedings of the 31st International Conference on Neural Information Processing Systems. Curran Associates Inc., Long Beach, California, USA, pp. 4768–4777.

Malone, B.P., McBratney, A.B., Minasny, B., Laslett, G.M., 2009. Mapping continuous depth functions of soil carbon storage and available water capacity. Geoderma 154(1), 138–152. https://doi.org/10.1016/j.geoderma.2009.10.007

Melillo, J.M., Frey, S.D., DeAngelis, K.M., Werner, W.J., Bernard, M.J., Bowles, F.P., Pold, G., Knorr, M.A., Grandy, A.S., 2017. Long-term pattern and magnitude of soil carbon feedback to the climate system in a warming world. Science 358(6359), 101–105. https://doi.org/10.1126/science.aan2874

Minasny, B., Malone, B.P., McBratney, A.B., Angers, D.A., Arrouays, D., Chambers, A., Chaplot, V., Chen, Z.S., Cheng, K., Das, B.S., Field, D.J., Gimona, A., Hedley, C. B., Hong, S.Y., Mandal, B., Marchant, B.P., Martin, M., McConkey, B.G., Mulder, V.L., O'Rourke, S., Richer-de-Forges, A.C., Odeh, I., Padarian, J., Paustian, K., Pan, G., Poggio, L., Savin, I., Stolbovoy, V., Stockmann, U., Sulaeman, Y., Tsui, C. C., Vågen, T.G., van Wesemael, B., Winowiecki, L., 2017. Soil carbon 4 per mille. Geoderma 292, 59–86. https://doi.org/10.1016/j.geoderma.2017.01.002

Mishra, U., Gautam, S., Riley, W.J., Hoffman, F.M., 2020. Ensemble Machine Learning Approach Improves Predicted Spatial Variation of Surface Soil Organic Carbon Stocks in Data-Limited Northern Circumpolar Region. Frontiers in Big Data 3, 528441. https://doi.org/10.3389/fdata.2020.528441

Morais, T.G., Teixeira, R.F.M., Domingos, T., 2019. Detailed global modelling of soil organic carbon in cropland, grassland and forest soils. PLOS ONE 14(9), e0222604. https://doi.org/10.1371/journal.pone.0222604

Moura-Bueno, J.M., Dalmolin, R.S.D., Horst-Heinen, T.Z., Grunwald, S., ten Caten, A., 2021. Environmental covariates improve the spectral predictions of organic carbon in subtropical soils in southern Brazil. Geoderma 393, 114981. https://doi.org/10.1016/j.geoderma.2021.114981

Mulder, V.L., Lacoste, M., Richer-de-Forges, A.C., Arrouays, D., 2016. GlobalSoilMap France: High-resolution spatial modeling of the soils of France to a depth of two meters. Science of The Total Environment 573, 1352–1369. https://doi.org/10.1016/j.scitotenv.2016.07.066

Qin, F., Zhao, Y., Shi, X., Xu, S., Yu, D., 2016. Sensitivity and uncertainty analysis for the DeNitrification–DeComposition model: a case study of modeling soil organic carbon dynamics at a long-term observation site with a rice–bean rotation. Computers and Electronics in Agriculture 124, 263–272. https://doi.org/10.1016/j.compag.2016.04.017

Rousseeuw, P.J., Hubert, M., 2011. Robust statistics for outlier detection. Wiley Interdisciplinary Reviews: Data Mining and Knowledge Discovery 1(1), 73-79. https://doi.org/

10.1002/widm.2
Schuur, E.A.G., McGuire, A.D., Schädel, C., Grosse, G., Harden, J.W., Hayes, D.J., Hugeli us, G., Koven, C.D., Kuhry, P., Lawrence, D.M., Natali, S.M., Olefeldt, D., Roma novsky, V.E., Schaefer, K., Turetsky, M.R., Treat, C.C., Vonk, J.E., 2015. Climate change and the permafrost carbon feedback. Nature 520(7546), 171–179. https://doi. org/10.1038/nature14338
Smith, J., Smith, P., Wattenbach, M., Zaehle, S., Hiederer, R., Jones, R.J.A., Montanarella, L., Rounsevell, M.D.A., Reginster, I., Ewert, F., 2005. Projected changes in minera l soil carbon of European croplands and grasslands, 1990–2080. Global Change Bi ology 11(12), 2141–2152. https://doi.org/10.1111/j.1365-2486.2005.001075.x
Smith, P., Smith, J.U., Franko, U., Kuka, K., Romanenkov, V.A., Shevtsova, L.K., Wattenb ach, M., Gottschalk, P., Sirotenko, O.D., Rukhovich, D.I., Koroleva, P.V., Romanen ko, I.A., Lisovoi, N.V., 2007. Changes in mineral soil organic carbon stocks in the croplands of European Russia and the Ukraine, 1990–2070; comparison of three models and implications for climate mitigation. Regional Environmental Change 7 (2), 105–119. https://doi.org/10.1007/s10113-007-0028-2
Tang, J., Cheng, H., Fang, C., 2017. The temperature sensitivity of soil organic carbon de composition is not related to labile and recalcitrant carbon. PLOS ONE 12(11), e0 186675. https://doi.org/10.1371/journal.pone.0186675
Torn, M.S., Trumbore, S.E., Chadwick, O.A., Vitousek, P.M., Hendricks, D.M., 1997. Mine ral control of soil organic carbon storage and turnover. Nature 389(6647), 170-173. https://doi.org/10.1038/38260
Trettin, C.C., Song, B., Jurgensen, M.F., Li, C., 2001. Existing soil carbon models do not apply to forested wetlands. General Technical Report SRS-46. U.S. Department of Agriculture, Forest Service, Southern Research Station, Asheville, NC, 10 pp. https: //doi.org/10.2737/SRS-GTR-46
van Gestel, N., Shi, Z., van Groenigen, K.J., Osenberg, C.W., Andresen, L.C., Dukes, J.S., Hovenden, M.J., Luo, Y., Michelsen, A., Pendall, E., Reich, P.B., Schuur, E.A.G., Hungate, B.A., 2018. Predicting soil carbon loss with warming. Nature 554(7693), E4–E5. https://doi.org/10.1038/nature25745
Wang, M., Zhang, S., Guo, X., Xiao, L., Yang, Y., Luo, Y., Mishra, U., Luo, Z., 2024. R esponses of soil organic carbon to climate extremes under warming across global biomes. Nature Climate Change 14(1), 98–105. https://doi.org/10.1038/s41558-023-0 1874-3
Wang, Y., Tao, F., Chen, Y., Yin, L., 2022. Interactive impacts of climate change and agri cultural management on soil organic carbon sequestration potential of cropland in China over the coming decades. Science of The Total Environment 817, 153018. h ttps://doi.org/10.1016/j.scitotenv.2022.153018
Weihermüller, L., Graf, A., Herbst, M., Vereecken, H., 2013. Simple pedotransfer functions to initialize reactive carbon pools of the RothC model. European Journal of Soil Science 64(5), 567-575. https://doi.org/10.1111/ejss.12036
Wiesmeier, M., Poeplau, C., Sierra, C.A., Maier, H., Frühauf, C., Hübner, R., Kühnel, A., Spörlein, P., Geuß, U., Hangen, E., Schilling, B., von Lützow, M., Kögel-Knabner, I., 2016. Projected loss of soil organic carbon in temperate agricultural soils in the

21st century: effects of climate change and carbon input trends. Scientific Reports 6, 32525. https://doi.org/10.1038/srep32525

Xu, L., He, N., Yu, G., 2019. A dataset of carbon density in Chinese terrestrial ecosystem s (2010s). China Scientific Data 4(1), 90-96. https://doi.org/10.11922/csdata.2018.00 26.zh

Xu, W., Yuan, W., 2017. Responses of microbial biomass carbon and nitrogen to experime ntal warming: A meta-analysis. Soil Biology and Biochemistry 115, 265-274. https: //doi.org/10.1016/j.soilbio.2017.08.033

Yan, C., Yuan, Z., Shi, X., Lock, T.R., Kallenbach, R.L., 2020. A global synthesis reveals greater sensitivity of soil carbon flux than carbon pools to warming. Journal of So ils and Sediments 20(3), 1208–1221. https://doi.org/10.1007/s11368-019-02513-1

Yan, Y., Wang, J., Tian, D., Luo, Y., Xue, X., Peng, F., He, J.-S., Liu, L., Jiang, L., Wan g, X., Wang, Y., Song, L., Niu, S., 2022. Sustained increases in soil respiration ac company increased carbon input under long-term warming across global grasslands. Geoderma 428, 116157. https://doi.org/10.1016/j.geoderma.2022.116157

Zhang, L., Heuvelink, G.B.M., Mulder, V.L., Chen, S., Deng, X., Yang, L., 2024. Using p rocess-oriented model output to enhance machine learning-based soil organic carbon prediction in space and time. Science of The Total Environment 922, 170778. htt ps://doi.org/10.1016/j.scitotenv.2024.170778

Zhang, L., Yang, L., Crowther, T.W., Zohner, C.M., Doetterl, S., Heuvelink, G.B.M., Wado ux, A.M.J.-C., Zhu, A.-X., Pu, Y., Shen, F., Ma, H., Zou, Y., Zhou, C., 2025. Ma pping global distributions, environmental controls, and uncertainties of apparent top soil and subsoil organic carbon turnover times. Earth System Science Data 17(6), 2605–2623. https://doi.org/10.5194/essd-17-2605-2025

Zhang, X., Xie, E., Chen, J., Peng, Y., Yan, G., Zhao, Y., 2023a. Modelling the spatiotem poral dynamics of cropland soil organic carbon by integrating process-based model s differing in structures with machine learning. Journal of Soils and Sediments 23 (7), 2816-2831. https://doi.org/10.1007/s11368-023-03516-9

Zhang, X., Zhao, Y., Xie, E., Peng, Y., Lu, F., 2020. Spatio-temporal change of soil organ ic carbon: progress and prospects. Journal of Agro-Environment Science 39(04), 67 3-679. https://doi.org/10.11654/jaes.2020-0031

Zhang, Z., Ding, J., Zhu, C., Chen, X., Wang, J., Han, L., Ma, X., Xu, D., 2021. Bivaria te empirical mode decomposition of the spatial variation in soil organic matter con tent: A case study from NW China. CATENA 206, 105572. https://doi.org/10.1016/ j.catena.2021.105572

Zhang, Z., Ding, J., Zhu, C., Wang, J., Ge, X., Li, X., Han, L., Chen, X., Wang, J., 202 3b. Historical and future variation of soil organic carbon in China. Geoderma 436, 116557. https://doi.org/10.1016/j.geoderma.2023.116557

Zhao, Y., Wang, J., Wang, S., Wu, H., Huang, S., Lu, C., 2016. Contributions of Wheat a nd Corn Residues to Soil Organic Carbon Under Fluvo-Aquic Soil Conditions—Ba sed on the Modified RothC Model. Scientia Agricultura Sinica 49(21), 4160–4168. https://doi.org/10.3864/j.issn.0578-1752.2016.21.010

Zhou, Z., Zhang, Z., Wang, M., Wang, K., Ai, J., Gill, A., Temirbayeva, K., Zhu, C., 202 5. Impact of future climate warming on soil organic carbon in China based on pr

ocess-based models. Climate Smart Agriculture 2(4), 100086. https://doi.org/10.1016/j.csag.2025.100086

Supplementary Files

This is a list of supplementary files associated with this preprint. Click to download.

- SupportingInformation.docx